Synthetic spectra for the secondary of the binary star system AA Dor with PHOENIX/3D

Synthetische Spektren für den Sekundärstern im AA Dor Doppelsternsystem mit PHOENIX/3D

Dissertation
zur Erlangung des Doktorgrades
an der Fakultät Mathematik, Informatik und Naturwissenschaften

Fachbereich Physik
der Universität Hamburg

vorgelegt von

Fiona Dorothea Elisabeth Prodöhl

HAMBURG
2021

Gutachter/innen der Dissertation:	Prof. Dr. Peter H. Hauschildt Prof. Dr. Travis S. Barman
Zusammensetzung der Prüfungskomission:	Prof. Dr. Robi Banerjee Prof. Dr. Travis S. Barman Prof. Dr. Peter H. Hauschildt Prof. Dr. Dieter Horns Prof. Dr. Jochen Liske
Vorsitzende/r der Prüfungskommission:	Prof. Dr. Jochen Liske
Datum der Disputation:	31-05-2021
Vorsitzender Fach-Promotionsausschus Physik:	Prof. Dr. Wolfgang Hansen
Leiter des Fachbereichs Physik:	Prof. Dr. Günter H. W. Sigl
Dekan der Fakultät MIN:	Prof. Dr. Heinrich Graener

Abstract

With the ongoing improvements of observational instruments it is possible to detect ever fainter objects and a larger variety of stars and exoplanets. To interpret this data, the demand for accordingly sophisticated theoretical models increases. Because many of these objects are not isolated, theoretical approaches that can include irradiation effects are of special interest.

As a step towards modelling the atmosphere of close binary stars and irradiated planets this work presents PHOENIX/3D models for the binary star system AA Dor.

At present it is not feasible to model these kind of objects in full level of detail in 3D with full hydrodynamics and radiative transfer coupling as well as full non-LTE treatment. Hence, a multi-step approach is presented in this work. A number of PHOENIX/1D models with and without external irradiation were patched together into a 3D structure, which we call 1.5D. The resulting hydrostatic structure was used to run irradiated PHOENIX/3D models.

With the PHOENIX/1D models, a slight atmosphere expansion due to local heating was found. Both 1.5D and 3D models were able to reproduce different observer perspectives. Limits for the 1.5D models were found near the terminator regions where 1D models fail to process the irradiation under low incident angles due to a lack of horizontal interactions. However, the 3D models are able to account for this and thus, transmission features at the limb of the nightside were found. Seven of the eleven identified secondary lines in the visual range listed in Hoyer et al. (2015) were found in these spectra and a dozen more lines suggested.

This shows, that upon further improvement of the input hydro-structure even more precise irradiation models can be delivered for studying close binary stars and extrasolar planets.

Zusammenfassung

Stetige Verbesserungen der Beobachtungsinstrumente machen es möglich, immer lichtschwachere Objekte und eine größere Vielfalt an Sternen und Exoplaneten zu detektieren. Damit diese Daten interpretiert werden können, werden dementsprechend differenziertere theoretische Modelle benötigt. Da viele dieser Objekte nicht isoliert vorkommen, sind theoretische Ansätze, die Bestrahlungseffekte berücksichtigen, besonders gefragt.

Als Schritt hin zum Modellieren von engen Doppelsternen und bestrahlten Planeten präsentiert diese Arbeit PHOENIX/3D Modelle für das Doppelsternsystem AA Dor. Da es zur Zeit nicht möglich ist, diese Art von Objekten in umfänglicher Detailliertheit zu modellieren, sprich in 3D mit kompletter Hydrodynamik- und Strahlungstransportkopplung sowie kompletter nicht-LTE Behandlung, wird hier ein mehrstufiges Verfahren dafür präsentiert. Dabei werden mehrere PHOENIX/1D Modelle mit und ohne externer Bestrahlung zu einer 3D Struktur, die wir 1.5D nennen, zusammengefügt. Die daraus resultierende hydrostatische Struktur wurde dann dazu benutzt bestrahlte PHOENIX/3D Modelle zu erzeugen.

Anhand der PHOENIX/1D Modelle konnte aufgrund der lokalen Erwärmung eine leichte Atmosphärenausdehnung festgestellt werden. Sowohl die 1.5D als auch die 3D Modelle waren in der Lage verschiedene Beobachterperspektiven wiederzugeben. Limitierungen für die 1D Modelle konnten nahe der Terminatorregion festgestellt werden. Hier scheitern die 1D Modelle daran die Einstrahlung unter flachen Einfallswinkeln zu verarbeiten, da keine horizontale Wechselwirkungen berücksichtigt sind. Die 3D Modelle sind hierzu jedoch im Stande, wodurch Durchstrahlungseffekte an den Rändern der Nachtseite sichtbar werden. Sieben der elf von Hoyer et al. (2015) gelisteten visuellen Linien des Sekundärsterns konnten mit den Modellen dieser Arbeit identifiziert werden und ein Dutzend weitere wurden vorgeschlagen.

Somit konnte gezeigt werden, dass mittels weiterer Verbesserung der Hydrostruktur noch präzisere Bestrahlungsmodelle für enge Doppelsterne und Exoplaneten erbracht werden können.

Contents

1 Introduction

We as humans have always been driven by curiosity. We long for answers to the big questions: Why do we exist? What is our place in the universe? Is the universe finite and if yes, how big is it? And is it possible that Earth is not the only planet with a biosphere? Due to our never ceasing thirst of knowledge, science has made huge progress on these questions throughout Earth's history. Since the first confirmation in 1992 (Wolszczan and Frail, 1992), we have been able to detect large amounts of exoplanets. As of April 14th, 2021 4375 exoplanets in 3247 planetary systems were known (NASA, 2021). A study from Petigura et al. 2013 found that "22% of Sun-like stars harbor Earth-size planets orbiting in their habitable zones". They defined "habitable zone" by conditions that permit surface liquid water. This percentage of incidence would suggest the Milky Way being home to eleven billion Earth-like planets based on statistical extrapolation. Unfortunately, it is not as easy to establish conditions under which planets are habitable for humans while suitable conditions for other forms of life could vary immensely from our understanding of a nice place to be. But even if an Earth-like planet in a so defined habitable zone is found, the conditions of life are also shaped by the abundance of chemical elements or molecules such as water, but also depend on the planet's albedo and its rotation (Yang et al., 2014).

With new instruments like TESS (launched 2018) and CHEOPS (launched 2019) and coming ones like PLATO (est. launch 2026) and ARIEL (est. launch 2028) it is going to be possible to detect even fainter objects and a larger variety of exoplanets. Direct detections by the Spitzer Space Telescope provided the first measurements of extrasolar planetary thermal emission (JPL, 2005) and NICMOS on the Hubble Space Telescope was used to spectroscopically study their atmosphere compositions and reveal planetary discs with modern image processing techniques by reanalysing

old image data (NASA, 2014, 2011). "To interpret this [observational] data, theorists have developed models for planet formation, orbital interaction and dynamics, evaporation due to stellar irradiation, atmospheric circulation and global heat transport, atmospheric structure and spectra, phase light curves, the equations of state of their interiors, molecular chemistry, radius evolution, and tidal effects, to name only a few topics." (Sozzetti, 2010)

The upcoming surge of observational data will allow us to do detailed statistics on exoplanets and their host stars. However, without sophisticated atmosphere models, those statistics will be misleading and all conclusions based on them may be wrong. Because of this, we need to improve our models further and verify them with currently available and well-studied objects. This involves variation of star-planet interactions and a first step towards this is the study of pre-cataclysmic variables.

Cataclysmic variables (CVs) are close binary stars comprising a white dwarf and a mass transferring secondary, that vary irregularly and strongly in brightness. Pre-CVs are previous to the mass exchanging phase with no distortions, yet. The close binary system chosen for this project is AA Doradus (AA Dor) with a hot subdwarf and a cooler late M to brown dwarf companion that will evolve eventually to a CV. We use this binary star system as a reference, but the utilized methods can be used for any close non-mass transferring binary system as well as for planet-star systems.

The atmosphere code PHOENIX allows to calculate spectra for a wide range of stars and substellar objects/planets. It is a good choice for this problem because it is capable of modelling the primary and the secondary star where the secondary can either be a star or a planet.

Pre-CV secondaries live in a much more extreme irradiation regime than many hot Jupiters because they are very close to their primary. AA Dor's primary is much hotter than the secondary so that the temperature gradient on the secondary between the irradiation-mediated heating on the dayside and the cool far side in addition to a separation of only 1.4 solar radii (around 7 and 14 times the primary's and secondary's

radius, respectively) is immense. This makes it a non-radialsymmetric case and using a 1D atmosphere code is not sufficient to account for features like transverse travelling light rays. This makes it a perfect object to study it with the Phoenix/3D code, comparing 1D to 3D and to observations.

Although the primary of AA Dor is studied in great variety (Kilkenny et al., 1981; Lynas-Gray et al., 1984; Rauch, 2000; Fleig et al., 2008), this is not the case for the secondary due to its much smaller contribution to the overall spectrum. Therefore, Rauch stated in 2000 that "almost nothing is known about the secondary". Fortunately, Vučković et al. (2008) were able identify first spectral lines originating from the secondary with VLT/UVES observations. Hoyer et al. (2015) were able to confirm these lines and add more with new XSHOOTER observations taken in 2014. The identified lines stem mainly from C II - III and O II. However, they did not succeed in extracting the spectrum of the cool side of the secondary. The first sophisticated, although still simple, atmosphere model for the secondary including irradiation and accounting for inhomogenities was presented by Vučković et al. (2016). They did a patch with four 1D NLTE models as a first step to understand the nature of the secondary more thoroughly.

In this work we are going to improve this understanding not only with a more detailed 1D patch structure, but also with a fully consistent 3D model. This work is a proof of concept for modelling 3D irradiated objects that starts with simplified models in local thermal equilibrium (LTE). This can be extended to non-LTE in future. Therefore, it is a first step towards an even better theoretical understanding of radiation transport in the extreme conditions of irradiated (sub)stellar objects.

Before we dive into our results we will explore the groundwork first. In Chapter 2 we introduce the binary star AA Dor that is being modeled in this work. We explain atmospheric modeling and our code PHOENIX including the central aspect of this

work: the irradiation mode. In Chapter 3 we describe how to build PHOENIX/1D and PHOENIX/3D models as well as how to patch so-called 1.5D models out of 1D models. In Chapter 4 we discuss the results, and finally give a short summery and a glimpse on possible future projects in Chapter 5.

2 Basics

In order to put our results into proper context, we will briefly summarize the most important theoretical fundamentals in this chapter. Section 2.1 introduces us to the most important works and findings related to our real life object, the binary star system AA Doradus (AA Dor). Then, we dive into atmosphere modeling in Section 2.2 to learn the groundwork of radiative transfer, because this is the theoretical base to our atmosphere modelling code PHOENIX, which we'll get to know in Section 2.3 including the irradiation mode which is the central part of studying irradiated objects. Irradiation effects play a significant role in a wide variety of binary systems, so, in favor of a more general description, the dominant source of the radiation will be referred to as the primary and the irradiated object as the secondary.
This Chapter is based on *Stellar atmospheres* by Mihalas (1970) and *Theory of Stellar Atmospheres: An Introduction to Astrophysical Non-equilibrium Quantitative Spectroscopic Analysis* by Hubenỳ and Mihalas (2015) if not stated otherwise.

Stars can be characterized by a multitude of parameters for instance their mass, temperature, color, brightness, size, and chemical composition. Among the better constrained observable characteristics, the effective temperature, surface gravity, as well as metallicity are typically utilized to categorize stars. The effective temperature T_{eff} of an object such as a star or planet is the temperature an idealized black body would have that emits the same total amount of electromagnetic radiation per surface area as the object. This temperature roughly corresponds to the local temperature in the lower photosphere. The surface gravity $\log g$ is the base-10 logarithm of the gravitational acceleration at the surface in cgs units ($\mathrm{cm/s^2}$). These quantities are directly related to the physical properties of a star such as mass, radius and luminosity. Luminosity is an absolute measure of electromagnetic energy emitted per unit of time. The chemical composition of a star can be determined from the star's spectrum. The

metallicity M/H is used as a measure of the total abundance of all heavy element species. Typically, this value is extrapolated from single element measurements and thus represents only a best rough approximation of reality. It is measured in reference to our sun as a base-10 logarithm by

$$[M_i/H] = log\frac{(n(M_i)/n(H))_*}{(n(M_i)/n(H))_\odot}\,, \tag{2.1}$$

where M_i refers to a single species and $n(M_i)$ is the number of elements of this species.

The details and the basics for the radiative transfer and irradiation processes can be found in Section 2.2.1. For more insights on stellar astronomy, the interested reader is referred to *Introduction to Stellar Astrophysics* by Böhm-Vitense (1989) and *The new cosmos: an introduction to astronomy and astrophysics* by Unsöld and Baschek (2001).

2.1 Binary Star System AA Dor

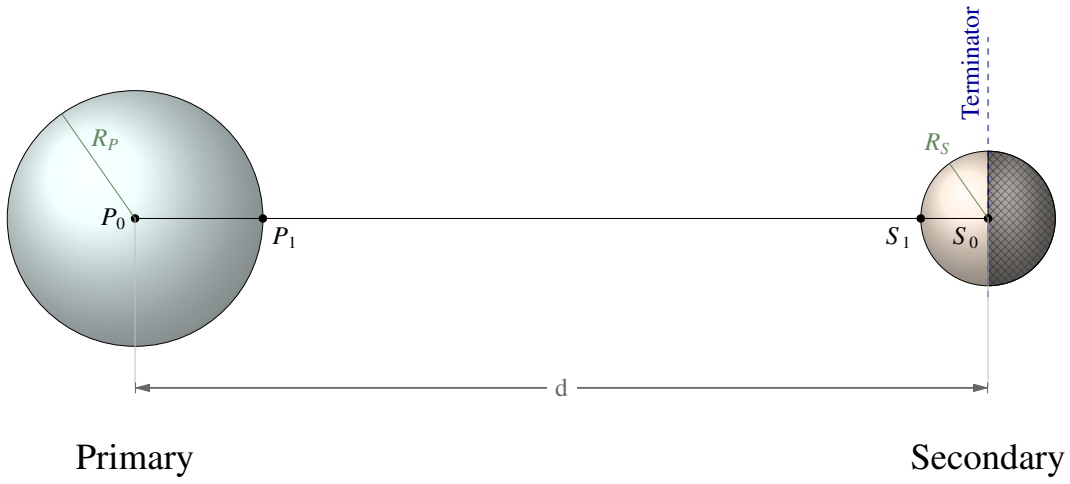

Figure 2.1: Geometry of the close binary system AA Dor with all dimensions to scale.

The close binary star system AA Doradus or AA Dor is also known as LB 3459 or HDE 269696. It belongs the the class of HW Viridis (Vir) type binaries. These eclipsing systems are known for very strong reflection effects due to the strong ultraviolet flux of the hot-subdwarf primary onto a much cooler M dwarf or brown dwarf. HW Vir type binaries can be devided into two subgroups: those similar to the prototype, with a core helium-burning subdwarf B primary, located in the extreme horizontal branch part of the H-R diagram. And those like AA Dor, which have a hotter and more evolved subdwarf OB primary, beyond the central helium exhaustion. With the new system found by Silvotti et al. (2021), the HW Vir subgroup, which AA Dor belongs to, obtained a third member. Further information on close binary stars and binary characteristics may be found in Hilditch (2001). For some more detailed eclipsing binary reading see Kallrath and Milone (2009).

AA Dor is located in the foreground of the Large Magellanic Cloud in a distance of 352 ± 23 pc from Earth. Thus, it clearly is a member of our galaxy. With an inclination of i=89.°21 ± 0.°30 it is observed edge-on. All currently known values of the AA Dor system can be found in Table 2.1. To date (Wolz et al., 2018) only 19 of HW Vir type systems have been identified, but AA Dor is the best-studied of them because it is one of the brightest ($m_V = 11.138$) HW-Vir type binary members with one of the longest periods ($P = 0.2615\,d$). Many more candidates are being uncovered by systematic surveys (e.g. EREBOS (Schaffenroth et al., 2017), Evryscope (Corcoran et al., 2019)), suggesting that these systems are not uncommon (see Heber (2016), and references therein).

Eclipsing binaries that irregularly alter in brightness by a large factor are so called cataclysmic variable (CV) stars and they mostly involve a white dwarf primary and a mass transferring secondary. AA Dor is previous to its CV stage (pre-CV), post common envelope evolution. The components are detached and no mass transfer occurs, yet. Hence, pre-CVs are exceptionally convenient objects to model binary star atmospheres.

Kilkenny and Hill (1975) were the first to report on slight variations of light curves for AA Dor. In 1978 Kilkenny et al. proved AA Dor to be a close, short-period, totally eclipsing binary. Early photometric investigations and light-curve analyses (Kilkenny et al., 1978, 1979) assumed both components to be hot subdwarfs or a hot white dwarf, but Paczynski and Dearborn (1980) and Conti et al. (1981) found that the contribution of the secondary mostly stems from reflected primary light and its intrinsic luminosity has to be very low compared to the primary. Thus, the dayside of the secondary is to be heated up to 20,000 K. Kudritzki et al. (1982) were the first presenting a non-local thermal equilibrium (NLTE) model for the primary, suggesting the primary has an effective Temperature of $T_{\mathrm{eff}} = 40,000$ K and a surface gravity of $\log g = 5.3 \pm 0.2$. Due to limited observational and computational resources uncertainties about evolution models and some parameters remain.

The prerequisites for renewed AA Dor investigations started with UVES (Ultraviolet and Visual Echelle Spectrograph) observations with ESO instruments in 2001, continuing with space-based FUSE (Far Ultraviolet Spectroscopic Explorer) data by NASA in 2003 and XSHOOTER observations at ESO in 2014. Additionally, modern data reduction methods and increasing computing power for more detailed theoretical models enhanced the research. Theoretical models could incorporate metal elements (Rauch, 2000) instead of the hitherto only H and He comprising models, except for Heber et al. (1988), who managed to add some C lines. The so-called g problem could be solved by Stark broadening improvements and a fuller consideration of the metal-line blanketing (Klepp and Rauch, 2011). This g problem arises due to discrepancies between the calculated masses derived by different methods (spectral analysis/ radial velocity measurements and eclipse curves). This results in surface gravity $\log g$ uncertainties, which could be narrowed by Klepp and Rauch to a value of $\log g = 5.46 \pm 0.05$. Studying eclipses from years 2000 to 2010 and 2011 to 2014 Kilkenny found that AA Dor has for its class of binary stars an interestingly stable orbit of $P = 0.2615397363(4)$ days (Kilkenny, 2011, 2014).

	Parameter	Symbol	Value
	Period	P	0.2615397363(4) d [3]
	Center-to-center distance	d	$1.41^{+0.09}_{-0.03}$ $R_\odot$ [4]
	Distance to Earth	D	(352 ± 23) pc [2]
	Magnitude	m_V	11.138
	Inclination	i	89°.21 ± 0°.30 [1]
Primary	Luminosity	L	120^{+15}_{-20} [2]
	Primary Mass	M_P	(0.46 ± 0.01) $M_\odot$ [5]
	Primary Radius	R_P	$0.2113^{+0.0346}_{-0.0195}$ $R_\odot$ [4]
	Prim. Eff. Temp.	$T_{eff,P}$	(42,000 ± 1000) K [2]
	Surface gravity	log g	(5.46 ± 0.05) cm s^{-2} [2]
	Radial velocity	K_P	(−39.63 ± 0.21) km s^{-1} [5]
Secondary	Secondary Mass	M_S	(0.079 ± 0.002) $M_\odot$ [5]
	Secondary Radius	R_S	$0.1112^{+0.0182}_{-0.0102}$ $R_\odot$ [4]
	Sec. Eff. Temp.	$T_{eff,S}$	∼ 2,500 K
	Surface gravity	log g_S	(5.276 ± 0.002) cm s^{-2} [5]
	Radial velocity	K_S	(231.3 ± 0.7) km s^{-1} [5]

Table 2.1: List of AA Dor Parameters taken from Hilditch et al. (2003)[1], Klepp and Rauch (2011)[2], Kilkenny (2014)[3], Hoyer et al. (2015)[4] and Vučković et al. (2016)[5]

Apart from Włodarczyk (1984), not much work has been done on the secondary before 2003 because the faint secondary spectrum is hidden by a dominant primary nature and it was not possible to isolate secondary features. Rauch and Werner made a new attempt to study the transit of the cool companion and created an animation of it that is available at Rauch and Werner (2011), but unfortunately without success in isolating secondary features. First identified spectral lines originating from the heated side of the secondary were found by Vučković et al. (2008). This list of lines were tripled by the work of Hoyer et al. (2015), but it still consists mainly of C II-III and O II emission lines.

Most recently, Vučković et al. (2016) published a 1D plane-parallel NLTE model for the secondary patching three models with different temperatures on the dayside to

account for the heterogeneity of this star. Several temperature inversion regions and an extension of the atmosphere was found. With radial velocities determined from the secondary's lines, the masses of this system could be determined with higher precision. A primary mass of (0.46±0.01) $M_\odot$ and a secondary mass of (0.079 ± 0.002) $M_\odot \mathrel{\hat{=}} 83\ M_{Jup}$ had been found. Chabrier and Baraffe (2000) stated that the minimum mass for hydrogen-burning is 0.075 $M_\odot$ and 0.083 $M_\odot$ for solar composition and $[M/H] = -2$, respectively. The metallicity of the secondary calculated by Vučković et al. (2016) was, with $[M/H] = -0.7$, surprisingly high. Hence, it remains unclear if the AA Dor secondary is a brown dwarf or late M dwarf.

Pre-CV stars need very good constrains on the secondary mass and its angular momentum to reliably model common-envelope evolution. Thus, due to the uncertainties about the evolution models, a controversy of its components remains (Vučković et al., 2016) and AA Dor continues to be an object of research. New space observations from the Transiting Exoplanet Survey Satellite (TESS) mission are presented by Baran et al. (2021) and they announce that from this mission there are even more observations to be expected in future.

2.2 Atmosphere Modeling

While fusion in the core of a star is the driving force for the star's light, the characteristic features of the spectrum are formed in the outermost layers of a star called the atmosphere. The atmosphere is a region with a finite probability of photon escape. This probability is strongly dependent on the photon wavelength. Thus, an important measure for atmosphere modeling is the optical depth

$$\tau_\nu = -\rho\, k_\nu\, dz, \tag{2.2}$$

with density ρ and total extinction k_ν (which can comprise scattering, absorption and line opacities and is dependent on the frequency $\nu = \frac{c}{\lambda}$ or wavelength λ of the light). Thus, the optical depth describes the degree of transparency of a material and is a more relevant quantity for photons than the geometric depth because it is a direct measure of the absorptivity of the material along its trajectory.

Within the atmosphere the radiation field is exposed to absorption, (re-)emission, and scattering effects which are shaped by (local) temperature, pressure, density, chemical composition of the star, and the total radiation flux. The source function S describes the removing and replacement of photons in a light beam that is travelling through gas and is defined by

$$S_\nu \equiv \frac{j_\nu}{k_\nu}, \tag{2.3}$$

with emission coefficient j_ν.

By definition the atmosphere by itself does not have any sources or sinks averaged over time and thus merely transports the total energy from the inside of the star to the outside. There are two major energy transport mechanisms within the atmosphere: radiation and convection. When basically all energy is transported by radiation this is called radiative zone. For a star like our sun radiative zone is satisfied to optical depths of order unity, below the atmosphere becomes unstable against convection due to hydrogen ionization. Typically, isolated stellar atmospheres are close to radiative equilibrium, where the energy inflows are balanced by the outflows.

Under the assumption of local thermal equilibrium, all local particle motion is described by Maxwell-Boltzmann-distribution and all occupations obey Saha-Boltzmann-equation where both rely on the local gas temperature T. Any deviation from that is called non-local thermal equilibrium (NLTE) and typically involves the solution of rate equations.

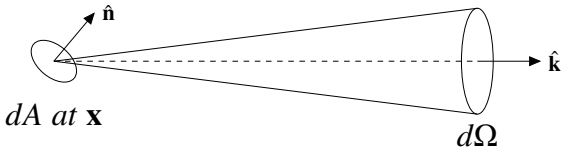

Figure 2.2: Visualization of the definition of the specific intensity $I_\nu(\hat{\mathbf{k}}, \mathbf{x}, t)$

The specific intensity I_ν is a measure of the energy dE that radiation of frequency ν transports when crossing a differential area dA within time dt observed under a differential solid angle $d\Omega$ as shown in Figure 2.2. It is defined by

$$dE = I_\nu(\hat{\mathbf{k}}, \mathbf{x}, t)\, \hat{\mathbf{k}} \cdot \hat{\mathbf{n}}\, \mathrm{d}A\, \mathrm{d}\Omega\, \mathrm{d}\nu\, \mathrm{d}t\ , \tag{2.4}$$

with the location $\mathbf{x}$ and the surface normal $\hat{\mathbf{n}}$ of dA and the direction $\hat{\mathbf{k}}$ of the surface element $d\Omega$.

The mean intensity $J_\nu(r)$ is defined by

$$\begin{aligned} J_\nu(r) &= \frac{1}{4\pi} \int I_\nu(r, \theta, \phi)\, \mathrm{d}\Omega \\ &= \frac{1}{4\pi} \int_0^{2\pi} \mathrm{d}\phi \int_0^{\pi} I_\nu(r, \theta, \phi)\ \sin\theta\, \mathrm{d}\theta\ , \end{aligned} \tag{2.5}$$

here applied to spherical coordinates (r, θ, ϕ)).

The radiation flux is defined as

$$F_\nu = \oint I_\nu(\mathbf{r}, \mathbf{n})\, \mathbf{n}\, \mathrm{d}\Omega\ . \tag{2.6}$$

In spherical coordinates this becomes

$$F = \int_0^{2\pi} \int_0^{\pi} I(\theta, \phi)\ \cos\theta\ \sin\theta\, \mathrm{d}\theta\, \mathrm{d}\phi\ . \tag{2.7}$$

For a spherical 1D model with a coordinate grid symmetric in ϕ and with $\mu = \cos\theta$ the formulas for the mean intensity and the flux becomes

$$J_\nu(r) = \frac{1}{2} \int_{-1}^{1} I_\nu(r, \mu)\, \mathrm{d}\mu \tag{2.8}$$

$$F = \int_{-1}^{1} I(\mu)\, \mu\, \mathrm{d}\mu\ . \tag{2.9}$$

2.2.1 Radiative Transfer

The radiative transfer (RT) describes photon interactions when travelling through matter. The 1D time independent RT equation in plane parallel geometry is given by

$$\mu \frac{dI_\nu}{d\tau} = I_\nu - S_\nu\ . \tag{2.10}$$

The simplest approach is to neglect scattering, so that the source function can be replaced by a blackbody. But while this significantly simplifies the problem, it is not very realistic. When taking scattering into account, the source function depends on the mean intensity. Thus, the RT equation is self-referential and needs to be computed iteratively. The most efficient method for this is the operator splitting method (Cannon, 1973).
Furthermore, the optical depth τ depends on the opacity k_ν which in turn affects the RT equation and thus the entire model atmosphere problem needs to be solved iteratively.

While the so far mentioned procedure describes the theoretical foundation, there are many different approaches to solve this. As this work is done with PHOENIX, the PHOENIX-specific details can be found in the following Section.
For more general in-depth discussions on atmosphere modelling and radiative trans-

fer see *Stellar atmospheres* by Mihalas (1970), *Theory of Stellar Atmospheres: An Introduction to Astrophysical Non-equilibrium Quantitative Spectroscopic Analysis* by Hubeny and Mihalas (2015) and *Radiative Transfer in Stellar Atmospheres* by Rutten (2003).

2.3 PHOENIX

PHOENIX is an atmosphere code that solves the radiative transfer (RT) for many different stellar types as well as substellar objects such as brown dwarfs or planets. It is available in 1D and 3D modes.
PHOENIX calculates the RT along many characteristic rays at discrete values of the optical depth τ and many different frequency points.
The PHOENIX method, described in the following, is illustrated in the flow-chart in Figure 2.3.
An initial guess for the temperature structure at the beginning of the first iteration is needed. This can be provided by previously calculated structures of similar objects or the assumption of a non-frequency dependent (gray approximation) RT can be made. With this temperature structure the equation of state (EOS) and the RT equation are solved.
In time-independent 1D, the results are checked for energy conservation. If this is not the case within the desired accuracy, the temperature is corrected at each layer in a way that the source function produces the correct flux. This process is repeated until the temperature corrections are small enough and the energy is conserved. In 3D strict reliance on time-independence and flux conservation is less meaningful, because this approach would smooth out any desired structures. Yet, these structures are often the reason why a 3D model is favored. Because the RT in PHOENIX/3D is already so computationally expensive, the calculation of consistent hydrodynamic would not only make the code much slower but it would make it so slow that the

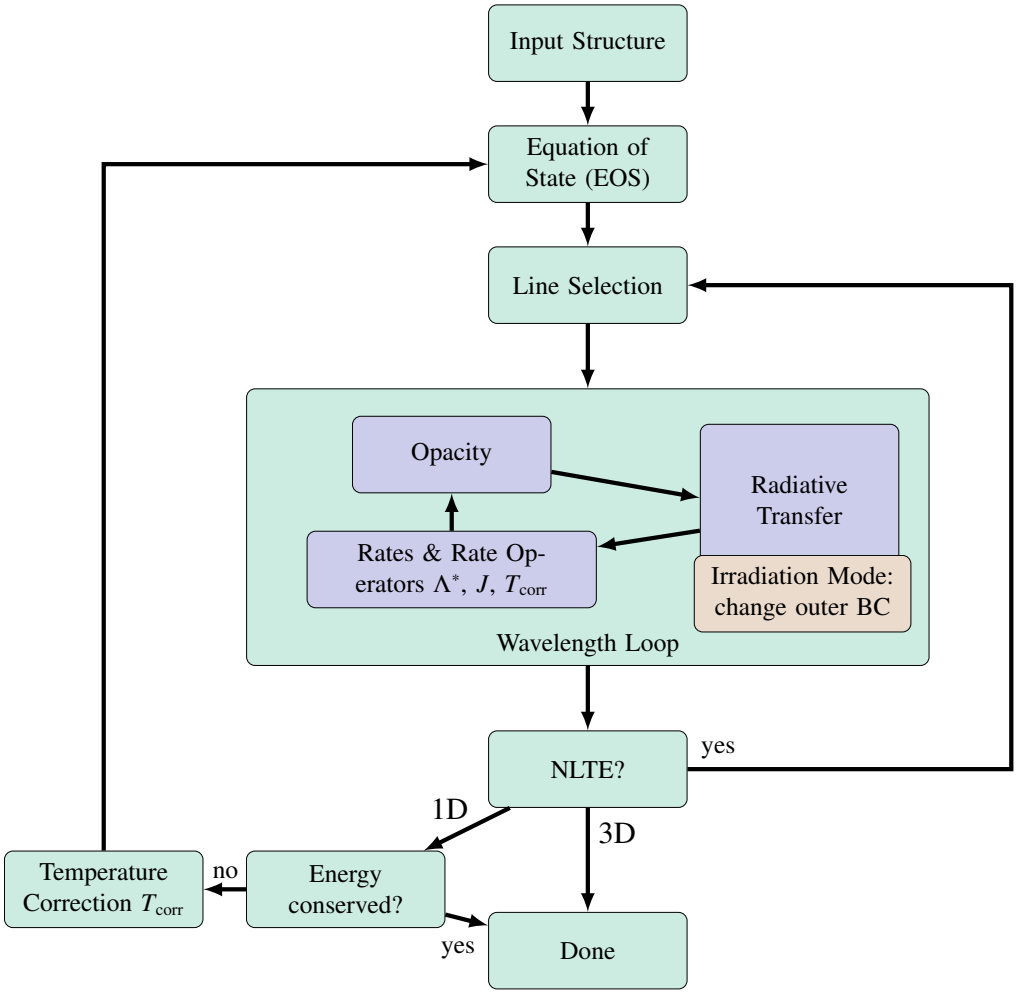

Figure 2.3: PHOENIX flow chart for 1D with temperature correction and 3D without including the additional irradiation mode changes (orange).

hydro-code could not relax from its initial conditions within a reasonable amount of time. Thus, presently PHOENIX/3D requires a pre-calculated hydrodynamic structure input.

Therefore, PHOENIX/1D differs from 3D by a temperature correction at the end of each iteration loop. While PHOENIX calculates the radiative transfer with characteristics in a grid along two directional dimensions for the intensity in every layer (1D) or every voxel (3D), additionally, in 3D the characteristics are coupled among adjacent voxels. Note that in PHOENIX/1D the flux at this 1D point on the surface of the

sphere corresponds to the flux over the whole sphere as seen by a distant observer if the star is radially symmetric. However, this is not true for the flux calculated in 3D. The 3D flux only represents the system if it does not deviate too much from static 1D equilibrium. Effects such as irradiation, oscillating or turbulent atmospheres could result in noticeable deviations.
For more details on PHOENIX see the paper series *A 3D radiative transfer framework* by Hauschildt and Baron (2006, 2009, 2010).

2.3.1 Irradiation Mode

Due to the fact, that this work focuses on irradiated objects, we will now discuss the irradiation mode included in PHOENIX more thoroughly. In contrast to stars treated in isolation, irradiated stars need to account for different boundary conditions and an additional temperature correction. The upper boundary condition defines the incoming intensities at the surface which becomes

$$\int_0^{2\pi} d\phi \int_{-1}^{0} I_\nu(\phi,\mu)\mu \, \mathrm{d}\mu = F_\nu^{\mathrm{inc}}(\tau = 0), \tag{2.11}$$

where F_ν^{inc} is the monochromatic flux from the primary incident upon the secondary surface. Most stellar and substellar objects can be assumed to be spherical. Thus, the radiation from the primary may be treated as a point source originating from the center of the primary (Wilson, 1990).
The flux received by the secondary at the substellar point (Figure 2.4 S_1) is given by

$$F^{\mathrm{inc}} = \left(\frac{R_P}{d - R_S}\right)^2 F_P \, . \tag{2.12}$$

The assumption that the angle δ between surface normal and primary center at a point on the secondary's surface is approximately the latitude θ of this point is valid if the

separation d is much larger than the radius of the secondary. Thus, the flux at an arbitrarily chosen point on the secondary's surface that is radially directed towards the center of the secondary may be written as

$$F^{\text{inc}} = \left(\frac{R_P}{d - R_S}\right)^2 F_P \mu \ . \tag{2.13}$$

As depicted in Figure 2.4 an observer at a region near the terminator may not see the whole primary because parts of the primary are below the horizon (red dashed line). However, in most cases, this penumbra effect is very small.

When taking into account the redistribution of energy through winds or convection a redistribution factor Q can be defined so that it takes values between 1 and 1/4, with 1 meaning no redistribution, 1/2 that the energy is uniformly distributed over the day hemisphere of the secondary and 1/4 total energy distributed over the entire sphere. This leads to the average incoming flux of

$$F^{\text{inc}}_{\text{avg}} = Q\left(\frac{R_P}{d - R_S}\right)^2 F_P \ . \tag{2.14}$$

To fulfill the radiative equilibrium constraint, the source function needs to be corrected at the end of each iteration. This correction is determined by the Unsöld-Lucy procedure (Lucy, 1964) which is based on the assumption that the ratios of the absorption means do not change much between each iteration step. However, for irradiated objects this procedure can become unstable if the external intensity is much bigger than the intrinsic energy. Stability can be ensured when splitting the intensity and its momenta into extrinsic and intrinsic components as well as the flux mean $\kappa_H H$, where H is the Eddington flux $H_\nu = \frac{1}{2}\int_{-1}^{1} I_\nu \mu \, d\mu$ and κ_H is the flux mean opacity $\kappa_H = \frac{1}{H}\int_0^\infty k_\nu \, d\nu$. The extrinsic properties don't change from iteration to iteration so they solely need to be computed once. Then, the radiative transfer equation is

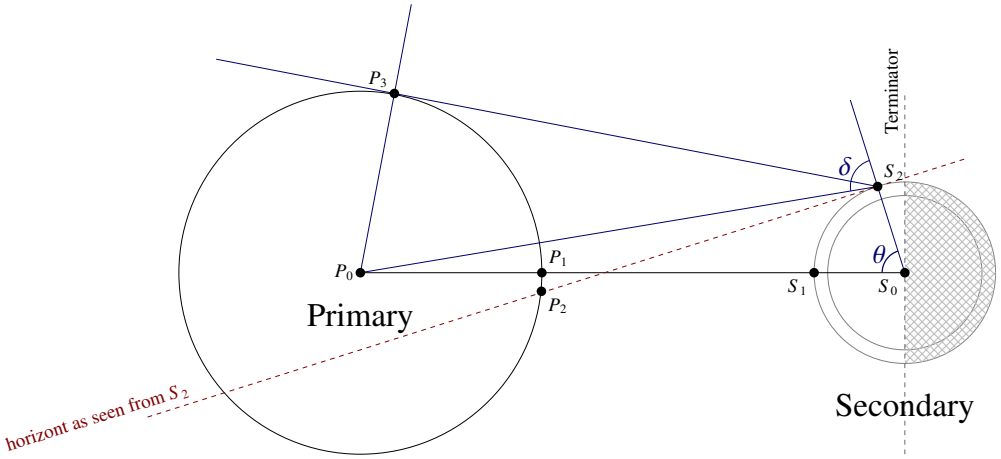

Figure 2.4: Geometry of a close binary. The angle δ between surface normal and primary center at point S_2 on the secondary's surface is assumed to be approximately the latitude θ of this point, if the separation d is much larger than the radius of the secondary. At this point S_2 near the terminator parts of the primary could lay below the horizon (red dashed line).

calculated twice every global iteration step. Firstly without extrinsic radiation field, secondly with it. The difference between the two different monochromatic intensities yields the intrinsic intensities. With these separately known intensities, the separate moments of the radiation field may be calculated and thus temperature corrections can be determined. A flow chart of the irradiation features within PHOENIX is depicted in Figure 2.3. Further details on irradiation in PHOENIX can be found in Hauschildt et al. (2003) and Barman (2002).

3 Methods

Modelling the AA Dor secondary in full level of detail in 3D with full hydrodynamics and radiative transfer coupling as well as full non-LTE treatment is presently not computationally feasible and thus we need to approach it by a simplified multi-step procedure.

As explained in Section 2.3 PHOENIX/3D does not comprise a hydrodynamic calculation routine and thus, we need to generate the hydrodynamic structure input externally. We calculated it by multiple PHOENIX/1D models that are post-processed to a so-called 1.5D composite. The geometry of our PHOENIX/1D models is explained in Section 3.1. In Section 3.2 we show how to build 1.5D models out of the 1D models and how to build the desired 3D input structure out of it. We talk about the 3D models in Section 3.3.

The models of this work are based on PHOENIX version 18.04 under LTE assumption and were run on the RRZ cluster Hummel (2015) for PHOENIX/1D and, due to an increased requirement for computation resources for PHOENIX/3D, on HLRN (2001). AA Dor parameters were chosen as listed in Table 3.1. Note that the secondary mass was chosen erroneously to be 0.187 $M_\odot$ instead of 0.079 $M_\odot$ but upon realisation time was lacking to redo all calculations. But even with this wrong number, especially due to uncertainties in secondary surface gravity $\log g$, but also due to all the simplifications at work, for instance LTE and low resolution, this work provides nonetheless a solid prove of concept of modeling close binary star systems with extreme conditions.

Parameter	Symbol	Value
Center-to-center distance	d	1.41 $R_\odot$ = 10^{11} cm
Primary eff. Temperature	$T_{\text{eff,P}}$	42,000 K
Primary Radius	R_P	0.21 $R_\odot$ = $1.46 \cdot 10^{11}$ cm
Primary Luminosity	L_P	$4.7 \cdot 10^{35}$ erg s^{-1}
Sec. eff. Temp.	$T_{\text{eff,S}}$	2,500 K
Sec. Radius	R_S	0.11 $R_\odot$ = $7.7 \cdot 10^9$ cm
Sec. surface gravity	$\log g$	5.50
Sec. Mass	M_S	0.187 $M_\odot$
Redistribution Factor	Q	0.5

Table 3.1: AA Dor Parameters used for the simulations

3.1 1D Simulation Setup

PHOENIX/1D's numerics functions best on the approach that the initial guess is already close to the final solution in order to secure convergence to the desired solution (Wichert, 2018). When adding external irradiation this assumption is shattered and thus the convergence of the temperature correction is no longer guaranteed. Robust convergence can be realized when approaching the desired binary star separation step by step when toggling to irradiation mode.

As AA Dor is tidally locked, the simple assumption is made that the secondary has one hemisphere completely at dark (nightside) and one hemisphere that is irradiated by the primary (dayside). Thus, the nightside can be represented by a model without irradiation mode with $T_{\text{eff,S}} = 2,500$ K and the dayside consists of several irradiation models with different incoming irradiation angles, all with the same internal temperature of $T_{\text{eff,S}} = 2,500$ K. The incoming radiation from the primary toggled in irradiation mode is simplified by a blackbody with the primary's effective temperature of $T_{\text{eff,P}} = 42,000$ K. Due to the very high effective temperature of the primary this is a fair assumption already.

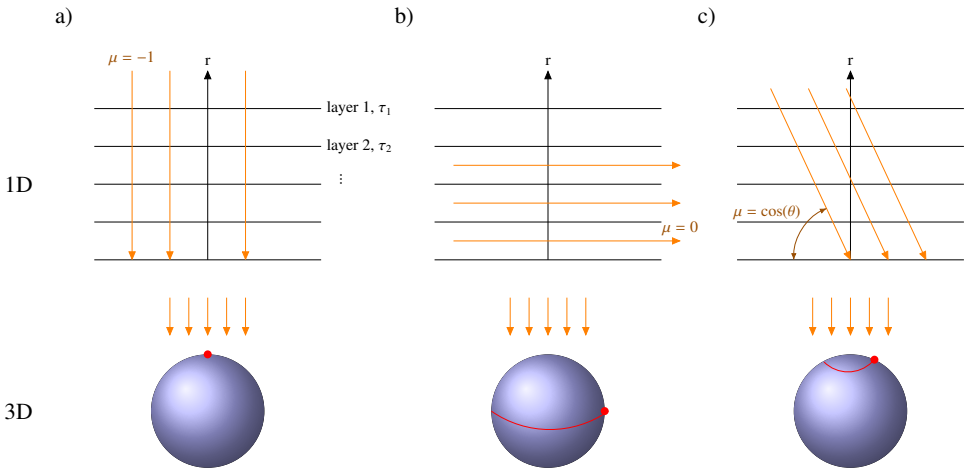

Figure 3.1: Geometry of the incoming radiation angle μ_{inc} in the irradiation mode a) at the substellar point b) at the terminator and c) somewhere in between. The upper part of this figure shows the incoming radiation (orange) angle μ_{inc} with respect to the atmospheric layers in the 1D mode. The lower part depicts the location on the secondary's 3D surface (red dots and lines of constant latitude) that is represented by this angle.

Definition of the incoming radiation angle

To simplify the geometry, the coordinate grid for the secondary is chosen in such a way that the north pole of the coordinate system coincides with the substellar point (the point on the secondary that is closest to the primary). Thus, the incoming radiation angle $\mu_{\text{inc}} = \cos\theta_{\text{inc}}$ is isotropic in longitude ϕ for any fixed latitude θ. The polar axis points from the center of the secondary towards the center of the primary, the $\phi = 0/180°$ plane lies in the plane of orbit (due to an inclination of the system of about 90°). The angle of the incoming radiation μ_{inc} is defined between the surface normal and the polar axis. While the coordinate system for the 3D model is clear, the transition of 1D model coordinates into 1.5D is not. Due to the fact that the coordinate system for the 1D models is chosen so that r points in the direction of the surface normal, the 1D models exhibit a rotation depending on the incoming angle μ_{inc} in reference to the 1.5D or 3D model. A visualization of the incoming radiation angle with respect to the 1D atmospheric layers chosen by PHOENIX and which location on a

1.5D or 3D model this incoming radiation angle corresponds to is shown in Figure 3.1. For simplicity the atmospheric layers are shown in plane-parallel mode, even though a spherical model was used.

3.2 From 1D To 1.5D

Because a 1D model alone cannot describe a strongly irradiated star, several 1D models with different irradiation angles are patched together to a quasi-3D, a so-called 1.5D model. This section describes how to transform from several 1D models to 1.5D one.

3.2.1 Calculate the grid for a unified outer radius

An automatic selection of the optical depth τ-grid is chosen in order to ensure optimal sampling. This is done with a reference continuum opacity at 12,000 Å and by setting the outer radius of the star at a gas pressure of 10^{-6} dyn cm^{-2}. Thereby, the spatial positions of the calculated atmosphere grid points vary from run to run. Therefore, especially when combining several 1D runs with different input parameters, the data points need to be interpolated onto the desired fixed spatial grid.
It is important to stress here that the angle μ_{RT} of the photon characteristics for which the radiative transfer (RT) is solved in PHOENIX/1D is dependent on the outer radius. $\mu_{\mathrm{RT}} = 1$ is defined for radiation that travels in the direction of the surface normal and $\mu_{\mathrm{RT}} = 0$ belongs to the outer radius where radiation travels horizontally to our atmospheric layers. Hence, with μ_{RT} dependent on the outer radius the 1D results with different outer radii have to be interpolated onto a new $\mu_{\mathrm{RT,new}}$ grid. We know that $\frac{r}{R} = \sin\theta_{\mathrm{RT}}$ with the radius r of the atmosphere layer, the outer radius R of this run, and $\mu_{\mathrm{RT}} = \cos\theta_{\mathrm{RT}}$ (Unsöld and Baschek, 2001). Thus, the angle $\mu_{\mathrm{RT,new}}$ for the

new outer radius value R_{new} can be calculated by

$$\mu_{\text{RT,new}} = \sqrt{1 - \sqrt{1 - (\mu_{\text{RT,old}})^2}\ \frac{R_{\text{old}}}{R_{\text{new}}}}\ . \tag{3.1}$$

3.2.2 Creating 1.5D spectra

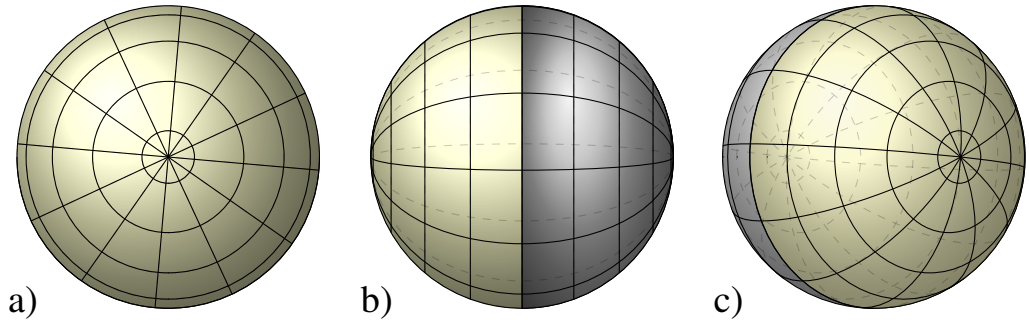

Figure 3.2: Geometry of secondary as seen from different observer perspectives. Irradiated (dayside) parts are colored in yellow, while the nightside is colored in gray. a) Full isoconcentric dayside rings are visible, b) day and night hemisphere are visible by half, c) sickle-shaped parts of the nightside are visible. Some lines of constant latitudes of the dayside are fully visible and others only by parts.

While the flux calculated by PHOENIX/1D sufficiently represents the spectrum as seen by a distant observer for radially symmetric stars this completely fails for our inhomogeneous secondary. Thus, the intensity values pointing in the direction of an observer need to be integrated over the visible part of the secondary (Equation 2.9). Different observer angles are depicted in Figure 3.2, showing that the visible part of the secondary can consist of different factions of night surface areas (unirradiated model, colored in gray) and day surface areas (irradiated models with different incoming radiation angle, colored in yellow).

The way PHOENIX/1D simulates the irradiation the most natural way to look at the secondary would be from the direction of the primary star so that for our tidally-locked system the intensities form iso-concentric rings around the substellar point (Figure 3.2 a)). Exactly in this position the primary occults the secondary, but shortly

before and after the occultation this phase is still observable.

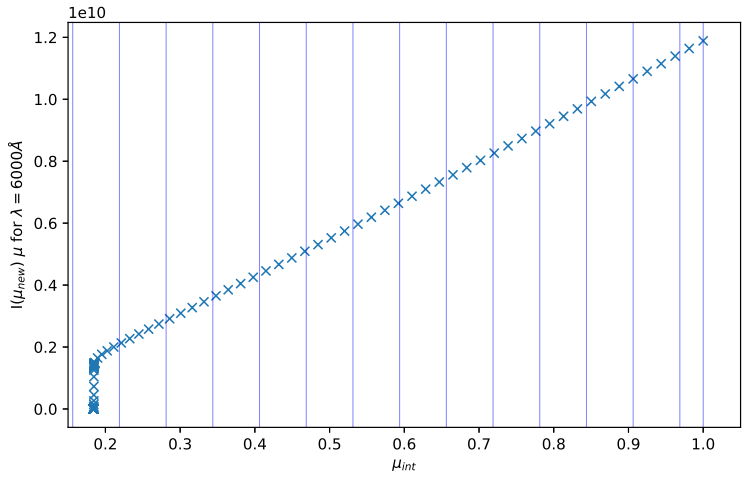

Figure 3.3: Visualisation of the 1.5D simple integration method for the nightside at $\lambda = 6000$ Å. The vertical lines mark the transitions between the different 1D models.

When calculating 1.5D spectra from 1D intensities, two different approaches are used to calculate the flux in this work. The first one is very simple and only works when observing the star frontally, as depicted in Figure 3.2 a) at full day or full night, the second approach is more general and applicable to all possible observation angles. Due to the fact that the 1D μ_{RT} angles are defined with respect to the surface normal, the intensity value for the angle pointing in the direction of the observer has to be calculated. For the simple method at full day or full night this angle coincides with the absolute value of the irradiation angle. Additionally, the visible part of the secondary is radially symmetric in ϕ, so integrating the intensities pointing in the direction of the observer over μ_{int} (these are the μ-values that are visible for a distant observer) is sufficient. The originally pointwise or in our radially symmetric case zero-width circled 1D results are broadened to rings so that neighboring irradiation angle rings touch. Figure 3.3 shows exemplarily a visualization of the intensity values for the nightside of the secondary at a wavelength of $\lambda = 6,000$ Å. To show the

transition between the different 1D models vertical lines are drawn. Obviously, due to it's patched nature, this is of great importance for the dayside model. Within every of these vertical intervals the corresponding intensity values pointing in the direction of the observer were chosen.

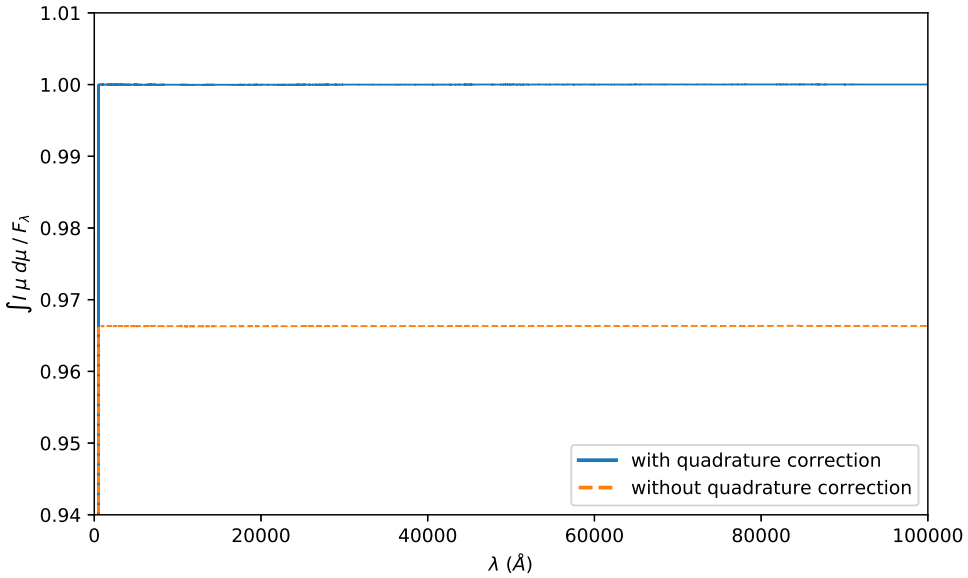

Figure 3.4: 1.5D nightside flux calculated by the simple method with (—) and without (- -) quadrature error correction as a fraction of the PHOENIX/1D-calculated flux.

As a consistency check, the integrated intensities for the isolated secondary are checked against the PHOENIX/1D-calculated flux because they must be identical. Due to the numerical integration quadrature nature, an error occurs when having only a small finite number of integration points. A good estimate for this error is the factor that $\int \mu \; d\mu$ differs from 1/2. The difference with and without this quadrature error correction is shown in Figure 3.4.

The second integration method is more general and considers an observer with the normalized coordinates $\vec{r}_{\text{obs}} = \begin{pmatrix} \sin\omega \sin\upsilon \\ \sin\omega \cos\upsilon \\ \cos\omega \end{pmatrix}$, where ω and υ are latitude and longitude in spherical coordinates, respectively. The angle α between this observer and an

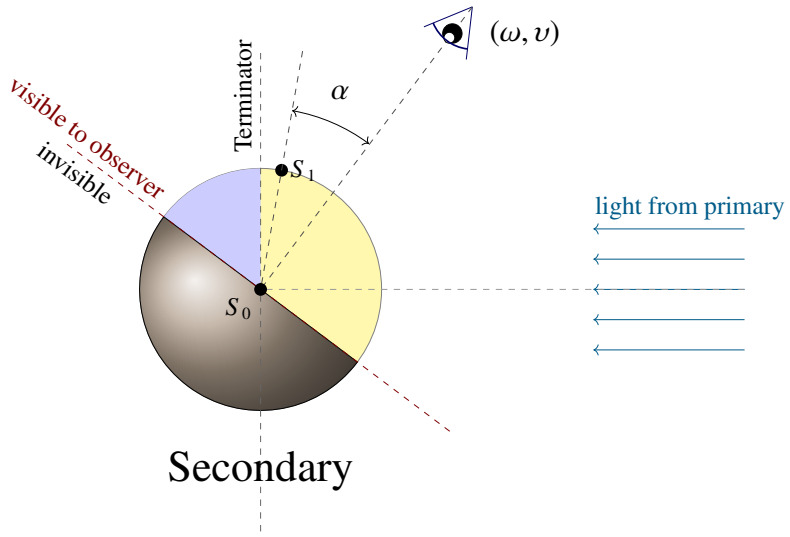

Figure 3.5: Geometry of the irradiated secondary with an observer at (ω, υ). The dayside of the secondary is colored in yellow, the nightside in light blue, the hemisphere that is not visible to the observer is colored in black. The angle between an arbitrary point on the secondary's surface $S_1(\theta_{\text{arb}}, \phi_{\text{arb}})$ and the observer is given by α.

arbitrary point on the secondary's surface given with $\vec{r}_{\text{arb}} = \begin{pmatrix} \sin\theta\cos\phi \\ \sin\theta\sin\phi \\ \cos\theta \end{pmatrix}$ (see Figure 3.5) can be calculated by simple vector geometry, resulting in

$$\begin{aligned} \cos(\alpha) &= \frac{\left|\vec{r}_{\text{obs}} \cdot \vec{r}_{\text{arb}}\right|}{\left|\vec{r}_{\text{obs}}\right| \cdot \left|\vec{r}_{\text{arb}}\right|} \\ &= \sin\omega\,\cos\upsilon\,\sin\theta\,\cos\phi + \sin\omega\,\sin\upsilon\,\sin\theta\,\sin\phi + \cos\omega\,\cos\theta\,. \end{aligned} \tag{3.2}$$

Then the flux is calculated by Equation 2.7 with the correct intensity values pointing towards the observer calculated with Equation 3.2. Thereby, the intensity values need to be interpolated because the intensity grid is discrete and the angle towards the observer are scarcely met.

As shown in Figure 3.6 this more general approach is more noisy than the simple method due to the interpolation process though it still matches the PHOENIX-calculated flux within a 3% margin.

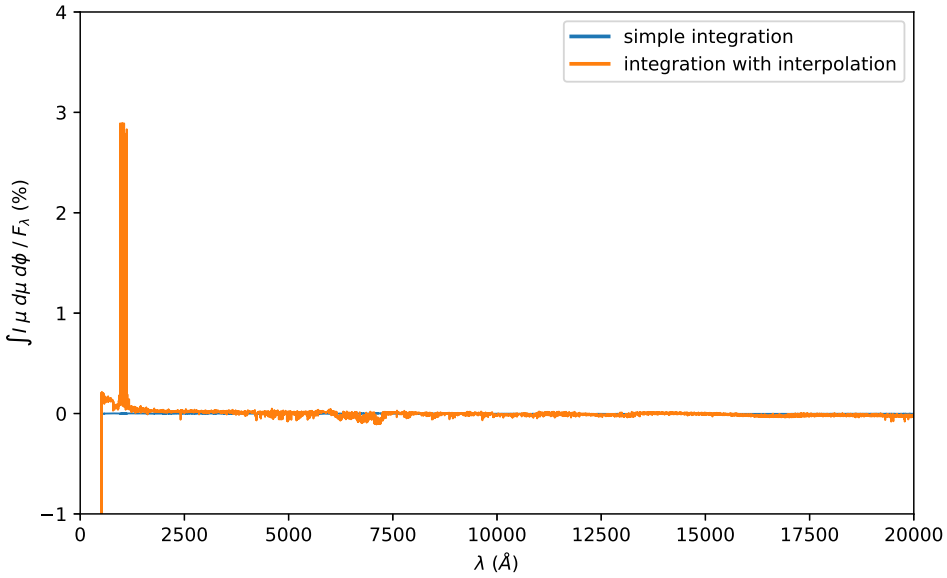

Figure 3.6: 1.5D flux calculated by the simple integration method (—) and the more general integration method with interpolation (—) as a percentage error in terms of the PHOENIX/1D-calculated flux.

3.2.3 Creating 3D input structure from 1D data

PHOENIX/3D is run on a pre-calculated temperature, gas pressure, and density structure which is created by merging the PHOENIX/1D results for different irradiation angles. As mentioned in Section 3.2.1 the different radii of the different PHOENIX runs for every τ-layer have to be interpolated onto one and the same radius grid in order to merge those runs to a 1.5D structure. First, an equally spaced θ grid between 0 and π with 33 values is chosen. Half of these correspond to the nightside and thus are represented by the unirradiated case. The other 16 θ angles are represented by runs with corresponding irradiation angles. The interpolated hydro structure is then, if necessary, smoothed, so that there are no steep gradients between two neighboring values. This is especially needed for the temperature because 1D models near the terminator failed and with the smoothing the 1D errors are not passed on to the 3D input structure. Due to the limitations of 1D, it is not possible to achieve a better transition region between dayside and nightside.

Figure 3.7 shows an example of a temperature profile that is interpolated onto a chosen radius grid that shows steep gradients.

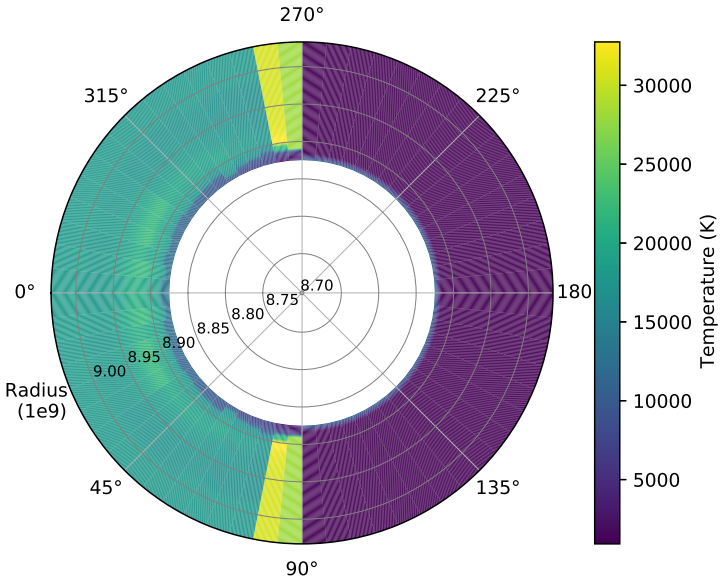

Figure 3.7: Example of a 1.5D temperature structure after interpolation

3.3 3D Simulation Setup

Phoenix/3D, while very sophisticated, is extremely heavy in consumption of time and hardware requirements, so to save computation time it is provided with a pre-converged hydro structure as an input. This is where our 1.5D structure is used.
Equivalent to our 1D models the 3D ones rely on LTE assumptions. Also, the same input parameters (shown in Table 3.1) were used. The irradiated 3D model was run on an irradiated 1.5D hydro structure and the unirradiated one on a unirradiated structure.
As mentioned in Section 2.2 the 3D flux is only a valid quantity for completely homogeneous stars. Here, it was solely used to check the unirradiated case for consistency.

For everything else the intensities were calculated by the formal solution (Eq. 2.10). The intensities are calculated for the spacial grid of the star (θ, ϕ) and for an observer direction grid (ω, υ) for every wavelength (λ): $I[\lambda, \theta, \phi, \omega, \upsilon]$. The spectrum was calculated by Equation 2.7 with the composite trapezoidal rule.

As arbitrary observer angles can be chosen, the results can be viewed from many different perspectives, see Figure 3.8. For this work three principal perspectives were chosen: full dayside (only the hemisphere that is facing the primary is visible ($\omega = 0, \upsilon = 0$)), half side (half of the day hemisphere and half of the night hemisphere are visible ($\omega = 90°, \upsilon = 0$)) and only the full nightside is visible (only the hemisphere that is facing away from the primary ($\omega = 180°, \upsilon = 0$)). Due to the symmetry in ϕ all relevant information can be found in this three perspectives.

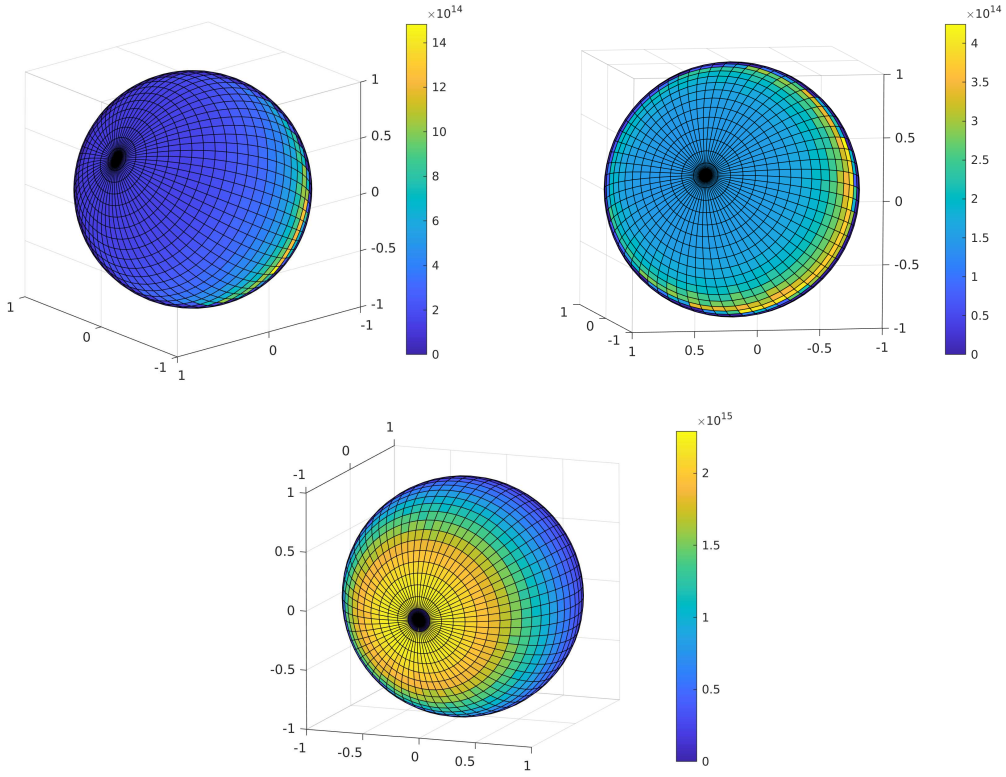

Figure 3.8: PHOENIX/3D flux of unirradiated model with unirradiated 1.5D hydro structure in spherical coordinates.

Test with unirradiated star

To test if our PHOENIX/3D setup runs correctly the same test as in Hauschildt and Baron (2009) was performed. As shown in Figure 3.9, the ratios F_ϕ/F_r and F_θ/F_r are close to zero, while the radial component of the flux F_r is non-zero. Thus, our PHOENIX/3D setup is correct.

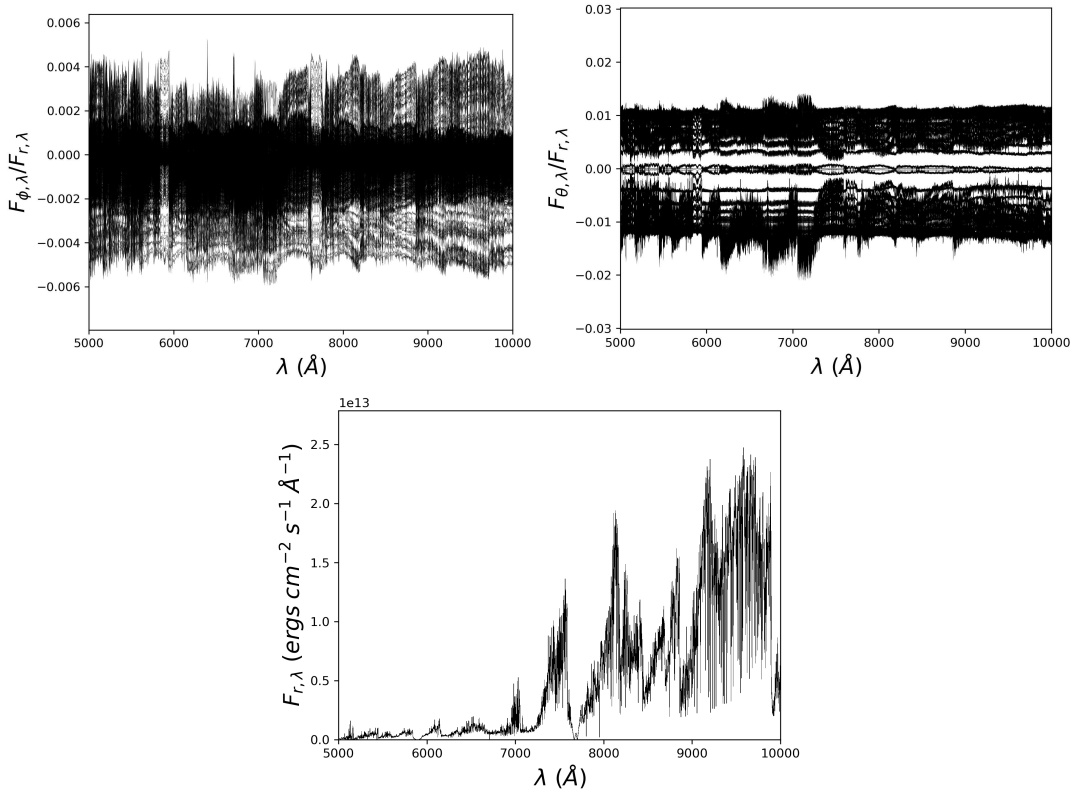

Figure 3.9: PHOENIX/3D flux of unirradiated model with unirradiated 1.5D hydro structure in spherical coordinates.

4 Results & Conclusion

Now we can finally dive into the results of the secondary models for the binary star system AA Dor done in this work. First, we will look at the 1D results in Section 4.1. Then, we will elucidate the 1.5D hydrostatic structure in Section 4.1.1. In Section 4.2 we will get to the 3D simulation results and compare these to the 1.5D ones in Section 4.3.

4.1 1D Simulations

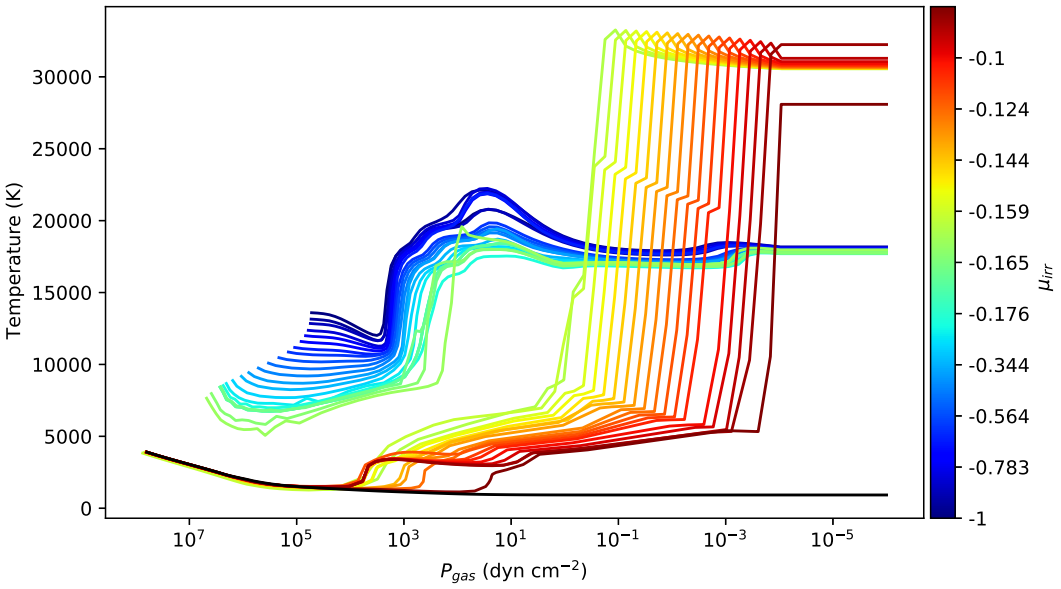

Figure 4.1: Temperature plot for an isolated star (black) and irradiation by different angles colored with regard to the incoming irradiation angle μ, with $\mu = -1$ corresponding to the substellar point and $\mu = 0$ the terminator. (Note that the color scale is not linear.)

Figure 4.1 shows the dependence of the temperature with respect to the gas pressure, which is reciprocal to the radial distance from the core, for the different incoming radiation angles explained in methods Section 3.1. The black line shows the tem-

perature for the unirradiated model. This is the expected decrease in temperature towards the outer regions of the secondary for an isolated star. For irradiation angles near the substellar point, which are colored in blue, we clearly see a temperature inversion with temperatures that reach up to about 22,000 K (up to 22,238.4 K for an irradiation angle of $\mu_{\mathrm{irr}} = -0.838$ / $\theta = 33.09°$). For irradiation angles near the terminator, shown in red, a huge temperature rise occurs rather suddenly. This shows the limitations of the 1D models, because these layers are receiving traverse light that is not passing through the core. The incoming energy needs to be reradiated under a very low angle, while being at very low density in these upper layers. Thus, the radiative equilibrium is broken and the temperature jump clearly is a model assumption artifact. Some models with irradiation angles below $\mu_{\mathrm{irr}} = -0.162$ / $\theta = 80.68°$ (near the terminator) had difficulties to converge or weren't able to converge at all. This value marks the transition region between the blue curves and the red ones.

Another arguable feature is the temperature discrepancy in the lower layers of the atmosphere. Due to the fact that all these models are made to describe one single star we would expect that the convection zone in depths of all models match each other. To correct this, entropy matching as described by Brett and Smith (1993) must be used.

In Figure 4.2 we find that different irradiation angles have their atmosphere layers at very different radii. This occurs due to the automatic radial grid construction by PHOENIX/1D with respect to the optical depth τ. A closer look to the impact onto the outer radius for different external irradiation angles is shown in Figure 4.3. The atmosphere expands up to 1300 km, which corresponds to an increase of 1.75%. In this work the outer radius is defined to be at a gas pressure of 10^{-6} dyn cm^{-2} and thus accounting for very thin atmosphere layers. Vučković et al. (2016) found a radius expansion of 600 km or 0.8%, but they didn't state what criterion they used to define the outer radius. As shown in Figure 4.4, the radius can vary a lot by means of the gas pressure. Thus,the agreement between our results and Vučković et al. may be perfect

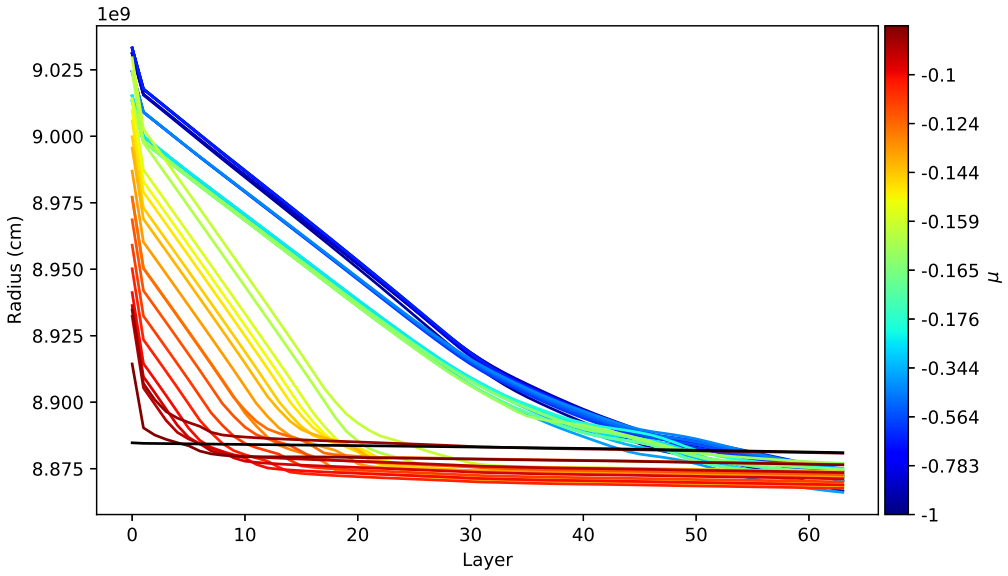

Figure 4.2: Radii of the atmospheric layers for an isolated star (black) and irradiation by different angles colored with regard to the incoming irradiation angle μ, with $\mu = -1$ corresponding to the substellar point and $\mu = 0$ the terminator. (Note that the color scale is not linear.) The layers are numbered from outside to inside with 0 corresponding to the outermost layer and 64 the innermost.

or completely off with the different definitions for the pressure at the outer radius.

Interestingly, the radius expands rather quickly and for irradiation angles μ_{irr} greater than -0.2 the maximal extension is almost reached.

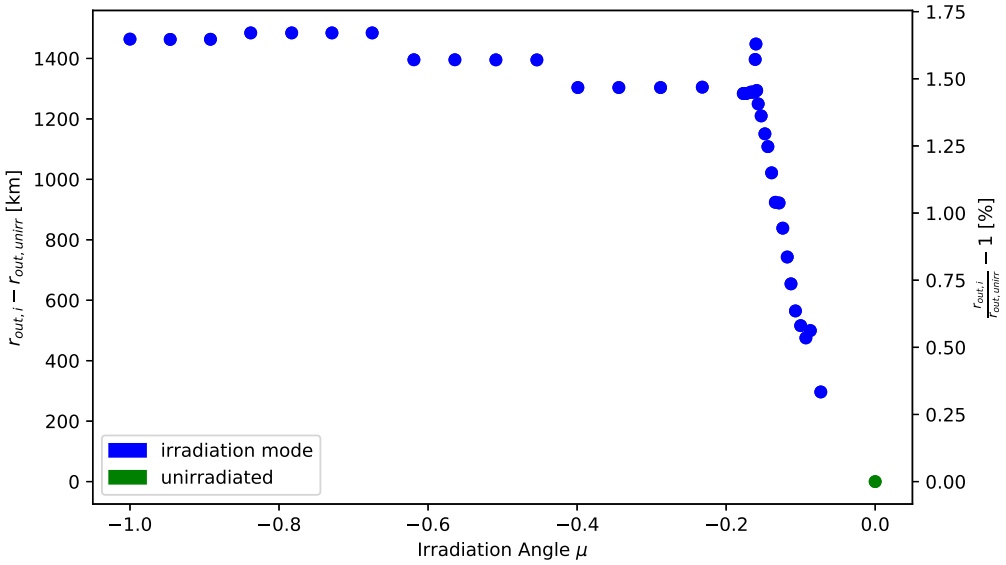

Figure 4.3: Outer radius of the secondary star for the isolated model (green) and irradiation by different angles (blue) in percent (right ordinate axis) and in absolute hight (left ordinate axis).

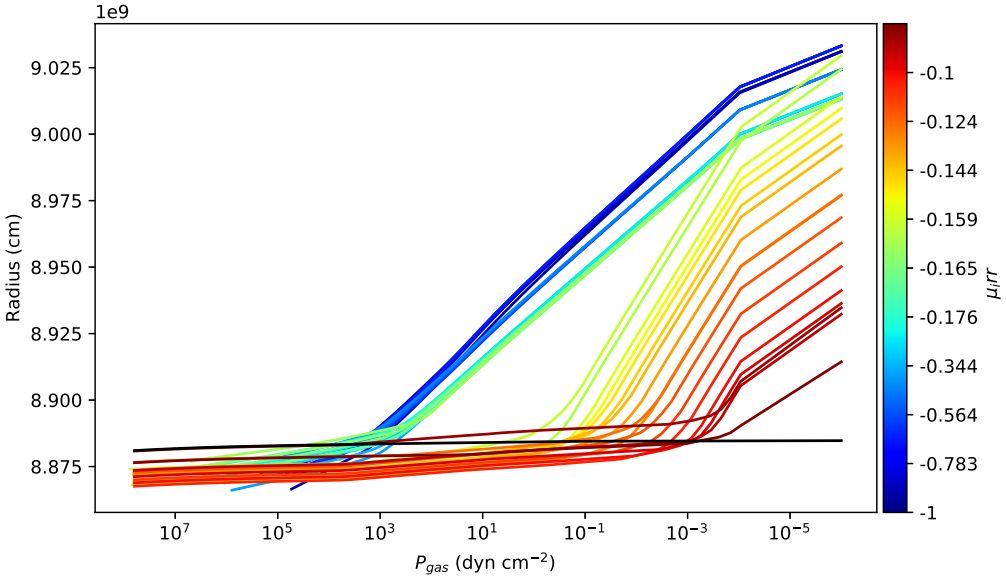

Figure 4.4: Gas pressure P_{gas} profile with respect to the radii for an isolated model (black) and various 1D models with different irradiation angles colored with regard to the incoming radiation angle μ, with $\mu = -1$ corresponding to the substellar point and $\mu = 0$ the terminator. (Note that the color scale is not linear.)

Figure 4.5 shows the density gas pressure relation for the different 1D models. As expected they are mostly linearly correlated in the log-log format. There are some transitions from the lower bluish line to the upper dark red ones. The bluish lines correspond to the ones in Figure 4.1 with the temperature inversion, black marks the unirradiated slope, while the red ones correspond to the irradiated models that exhibit the steep temperature rise in the outer atmosphere regions.

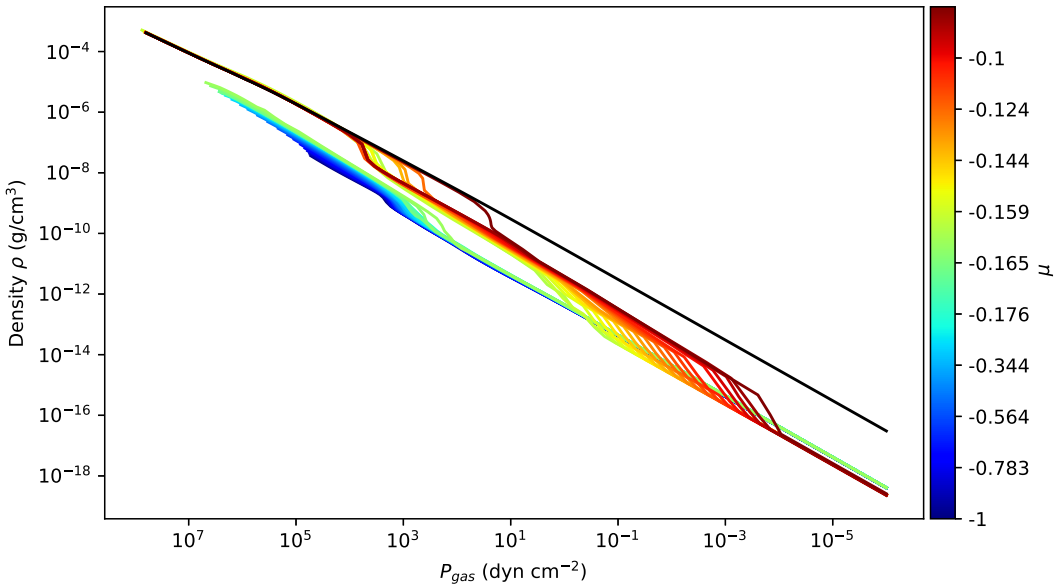

Figure 4.5: Density ρ and gas pressure P_{gas} profiles for 1D calculations with irradiation by different angles colored with regard to the incoming irradiation angle μ, with $\mu = -1$ corresponding to the substellar point and $\mu = 0$ the terminator. (Note that the color scale is not linear.)

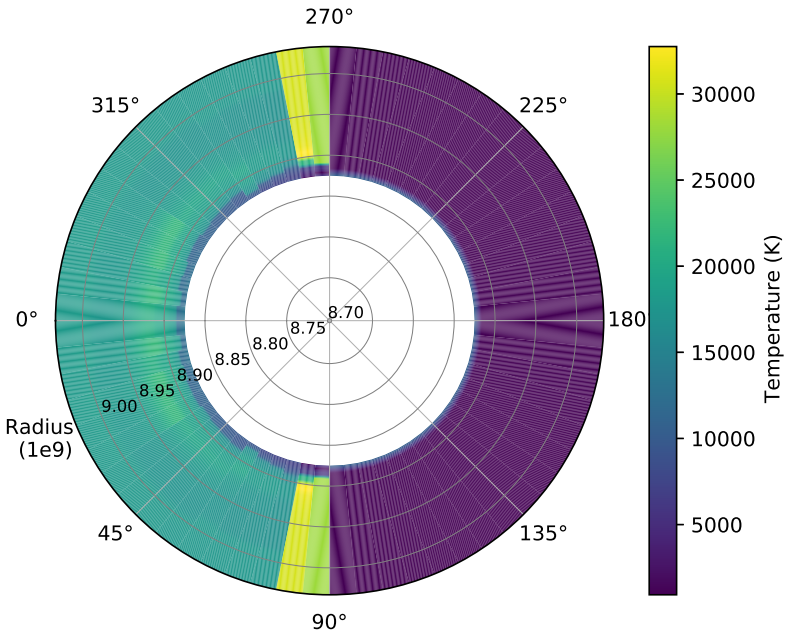

Figure 4.6: 1.5D temperature profile patched from 17 different 1D calculations with different irradiation angles for the dayside (left half of the ring) and an isolated model for the nightside (right) interpolated onto the same radius grid. The the secondary is sliced through $\phi = 90°/270°$. The profile is radialsymmetric in ϕ.

4.1.1 1.5D Hydrostatic structure

As explained in Section 3.2.3, the results of 17 different 1D models were combined to create a 1.5D hydrostatic structure. Figure 4.6 depicts this combined temperature structure, interpolated onto the same radius grid. The 3D secondary is sliced in half along the 90/ 270° longitude plane. Thus, the inner layers of the secondary with half night and half day structures become visible. The nightside remains cool, while the day side is heated up. A classical temperature inversion is clearly visible. As already discussed with Figure 4.1, regions towards the terminator are not well represented by our 1D models. Thus, unrealistically high temperatures occur in these regions. These artifacts have been straightened out by Gauss smoothing as depicted in Figure 4.7.

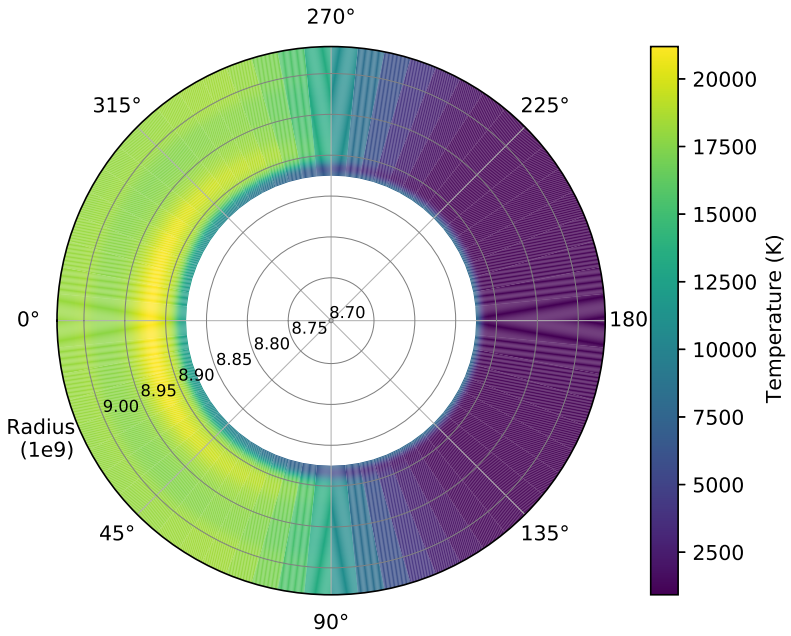

Figure 4.7: Gauss smoothed 1.5D temperature profile patched together from 17 different 1D calculations with different irradiation angles for the dayside (left half) and an isolated model for the nightside (right) interpolated onto the same radius grid. The the secondary is sliced through $\phi = 90°/270°$. The profile is radialsymmetric in ϕ.

Figure 4.8 shows the 1.5D structure for the gas pressure which is smoothed with a Gauss kernel in Figure 4.9. Because the density and gas pressure profiles behave very similar, only the smoothed version for the density is shown (Figure 4.10). The smoothed versions of the temperature, the gas pressure and the density were used as input for the PHOENIX/3D runs.

This simplification with exactly one hemisphere at night (unirradiated model) and the other hemisphere consisting of several models with different incoming irradiation angles doesn't take into account horizontal heat flows like wind and other global circulation effects. Yet, the applied Gauss smoothing softens up the sharp day-night transition at the terminator and thus accounts slightly for local commingling.

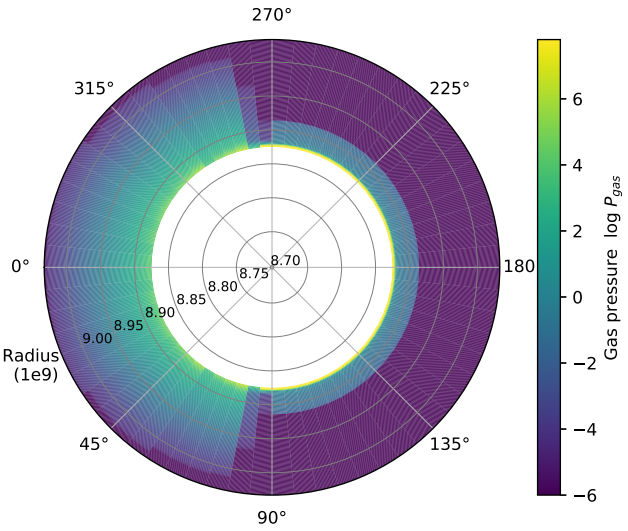

Figure 4.8: 1.5D logarithmic gas pressure profile patched from 17 different 1D calculations with different irradiation angles for the dayside (left half of the ring) and an isolated model for the nightside (right) interpolated onto the same radius grid. The the secondary is sliced through $\phi = 90°/270°$. The profile is rotational symmetric in ϕ.

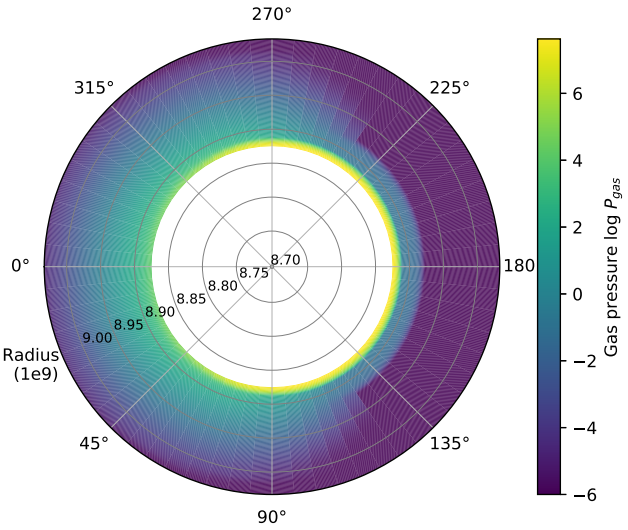

Figure 4.9: Gauss smoothed 1.5D logarithmic gas pressure profile patched from 17 different 1D calculations with different irradiation angles for the dayside (left half of the ring) and an isolated model for the nightside (right) interpolated onto the same radius grid. The the secondary is sliced through $\phi = 90°/270°$. The profile is rotational symmetric in ϕ.

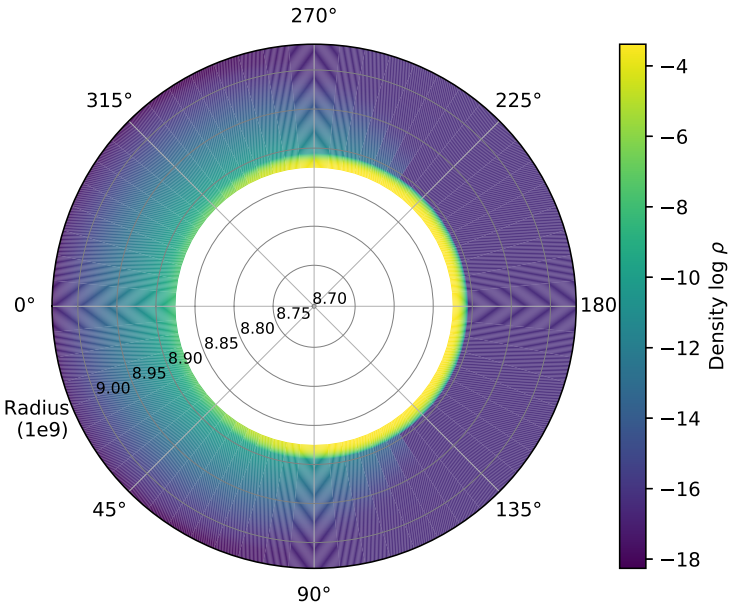

Figure 4.10: Gauss smoothed 1.5D logarithmic density profile patched from 17 different 1D calculations with different irradiation angles for the dayside (left half of the ring) and an isolated model for the nightside (right) interpolated onto the same radius grid. The the secondary is sliced through $\phi = 90°/270°$. The profile is rotational symmetric in ϕ.

4.1.2 1D and 1.5D Spectra

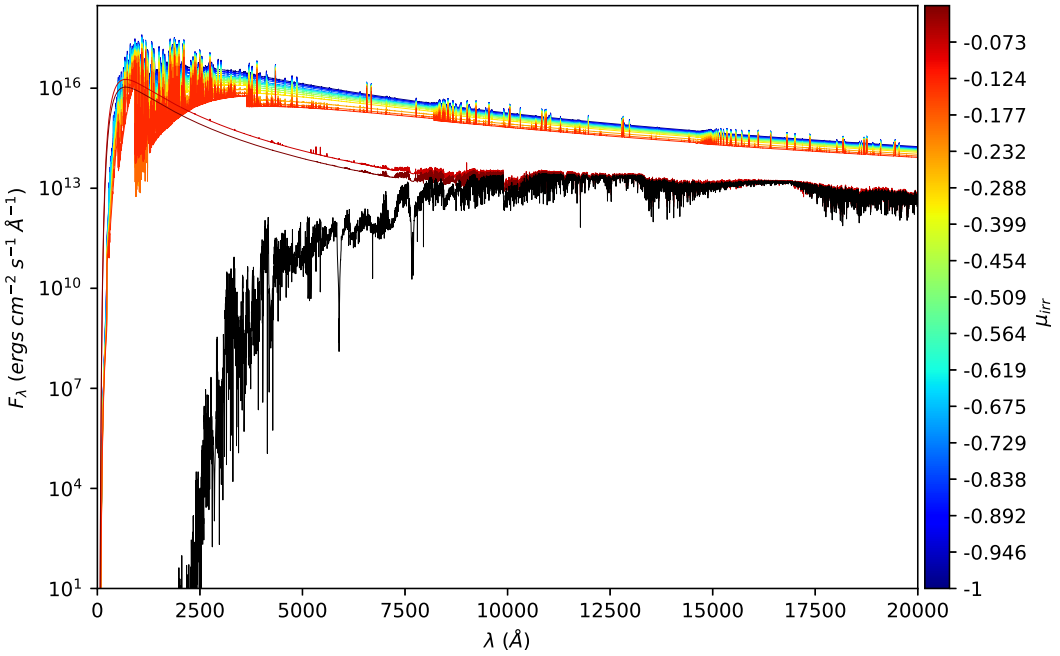

Figure 4.11: Spectra for different 1D models. The isolated star model is colored in black, the irradiation models are colored with regard to the incoming irradiation angle μ_{irr}, with $\mu_{\mathrm{irr}} = -1$ corresponding to the substellar point and $\mu_{\mathrm{irr}} = 0$ the terminator. (Note that the color scale is not linear.)

Figure 4.11 shows the spectra for the 17 different 1D models that were used to create the 1.5D hydro input structure. The spectra for the models with irradiation shift as expected towards a blackbody of higher temperatures. Again, the spectra for the models near the terminator look very different from the other irradiation spectra. They resemble a general blackbody, which is caused by the blackbody irradiation input with an temperature of 42,000 K and thus the maximum of these curves is as expected at a wavelength of $\lambda = 690$ Å. This can be an artifact of the artificial 1D traits already seen and discussed in Section 4.1, but it is also typical for very thin atmospheres, where most gas species are ionized. The unirradiated spectrum demonstrates mostly absorption features, while the irradiated spectra indicate lots of emission features. These spectra are theoretical and are not observable, as they

only resemble the spectra for single points on a 3D sphere. As explained in Section 3.2.2, the intensities of the different models have to be integrated over the visible hemisphere with two different methods.

The differences between the simple integration method and the interpolation method, as described in Section 3.2.2, are shown in Figure 4.12 for the full dayside. The simple integration has a slightly smaller flux than the interpolated one but not by a constant scaling factor, which can be seen in the lower part of this figure where the ratio of simple to interpolated integration is shown. There are no direct full dayside observation due to the fact that the secondary spectrum cannot be disentangled from the primary's so easily and that the secondary is hidden by the primary during the phase where the full daysides should be visible. Unfortunately, this makes it yet impossible to figure out which of the models is closer to reality.

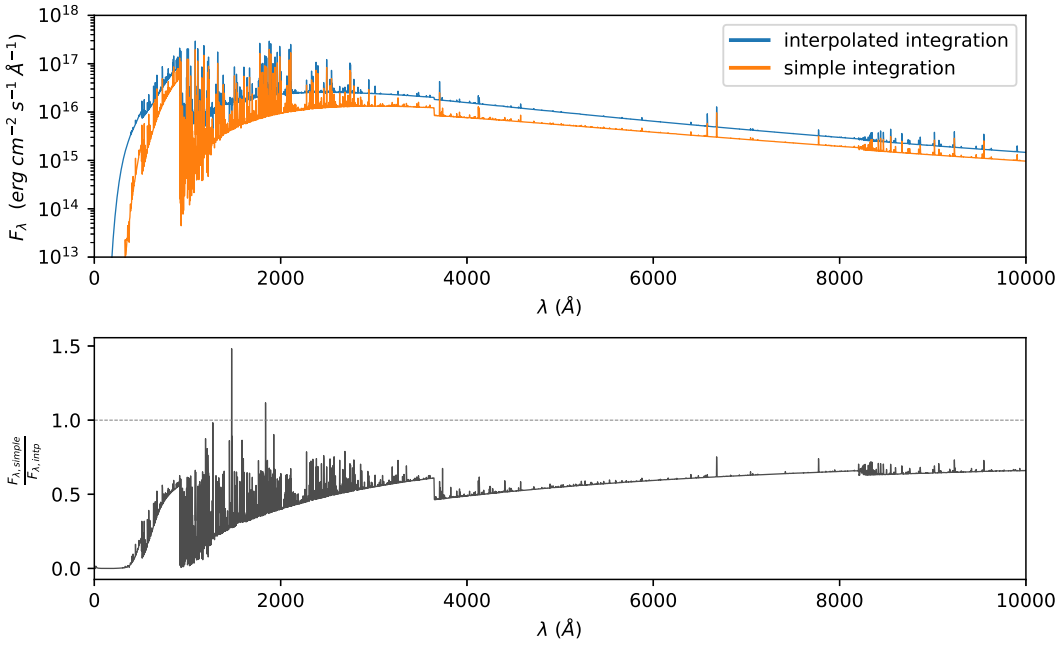

Figure 4.12: 1.5D spectra for the dayside for the simple and interpolation integration methods. The absolute flux is shown in the upper panel, the ratio of simple to interpolation method is shown in the lower panel.

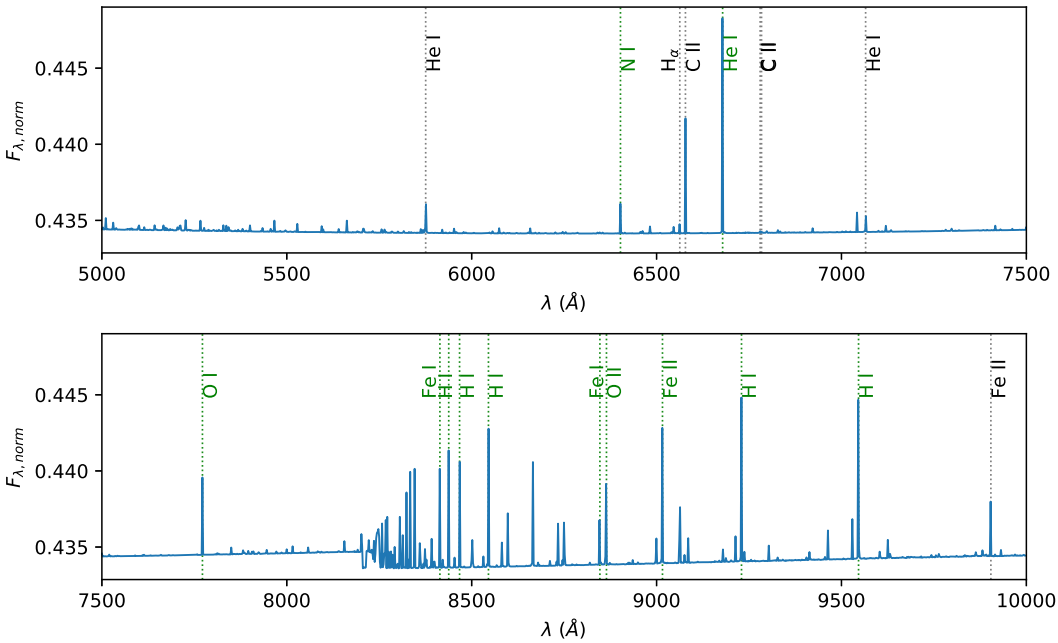

Figure 4.13: 1.5D normalized dayside spectrum shifted to air wavelengths with matching lines presented by Hoyer et al. (2015) (black) and lines identified in this work (green).

In Figure 4.13 a normalized dayside spectrum is presented with corresponding ion emission lines shown in black matching those given in Hoyer et al. (2015) and new lines suggested in this work in green. Due to the fact that the PHOENIX's output is given in vacuum wavelength, a vacuum-to-air shift was applied. Detailed wavelength values for the lines can be found in Table 4.1.

$\lambda_{\text{model,vac}}$ [Å]	$\lambda_{\text{model,air}}$ [Å]	$\lambda_{\text{obs/NIST}}$ [Å]	Ion	In Hoyer et al. (2015)
5878	5876.37	5875.63	He I	✓
6404	6402.23	6402.36	N I	
6564	6562.19	6562.82	H_α	✓
6580	6578.18	6578.06	C II	✓
6680	6678.16	6678.65	N I	
6782	6780.13	6780.50	C II	✓
6786	6784.13	6783.83	C II	✓
7068	7066.05	7065.32	He I	✓
7774	7771.86	7771.94	O I	
8416	8413.69	8414.09	Fe I	
8440	8437.68	8437.95	H I	
8470	8467.67	8467.26	H I	
8548	8545.65	8545.38	H I	
8848	8845.57	8846.74	Fe I	
8866	8863.57	8864.51	O II	
9018	9015.53	9015.99	Fe II	
9232	9229.47	9229.7	H I	
9548	9545.38	9546.2	H I	
9906	9903.28	9904.06	Fe II	✓

Table 4.1: Table of emission lines found in the dayside spectrum of the secondary in this work (highlighted in green) and in Hoyer et al. (2015).

The nightside was analyzed accordingly. Figure 4.14 and Table 4.2 show the normalized spectrum and the identified absorption lines for the nightside. These are mainly alkali lines, which are very common in observations of cool substellar objects (Kirkpatrick et al., 1999; Johnas, 2007).

For further comparison with observations, models with higher spectral resolution are needed. Due to the fact that this is the first prove-of-concept approach of this method, there are no automatic routines to create the 1.5D spectra, yet. So as of now, the procedure is very time consuming, but it is very much possible to automatize it for faster future applications.

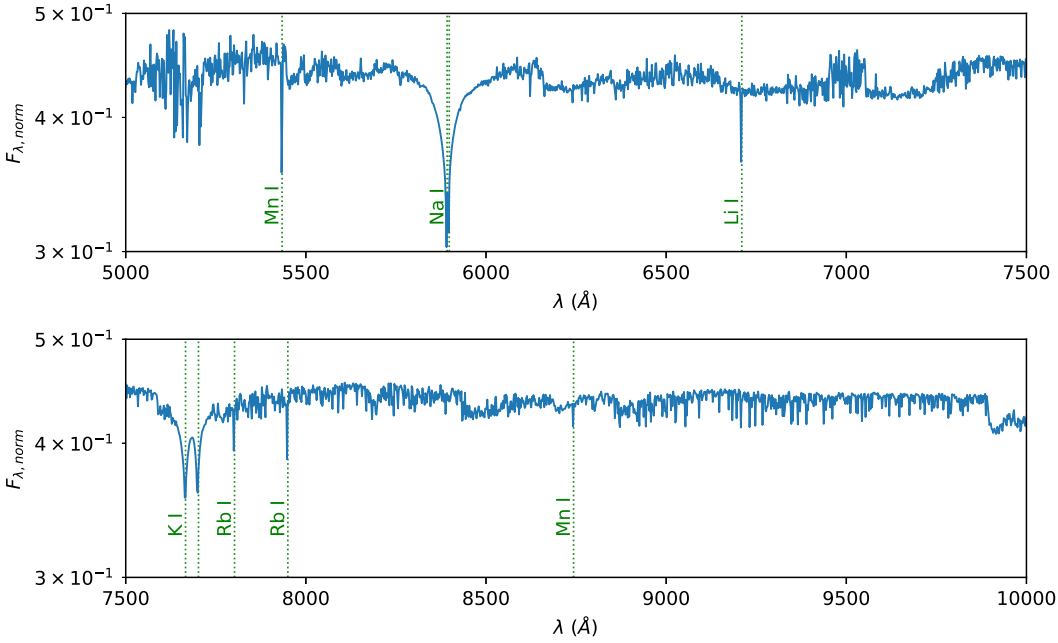

Figure 4.14: 1.5D normalized nightside spectrum shifted to air wavelengths with identified absorption lines.

$\lambda_{\text{model,vac}}$ [Å]	$\lambda_{\text{model,air}}$ [Å]	λ_{NIST} [Å]	Ion
5434	5432.49	5432.54	Mn I
5892	5890.37	5889.96	Na I
5898	5896.37	5895.93	Na I
6710	6708.15	6707.78	Li I
7667	7664.89	7664.89	K I
7701	7698.88	7698.96	K I
7802	7799.85	7802.47	Rb I
7950	7947.81	6787.21	Rb I
8743	8740.60	8743.56	Mn I

Table 4.2: Table of lines found in the nightside spectrum of the secondary in this work

4.2 3D Simulations

As explained in the methods Section 3.3 the flux for the unirradiated model was tested for correctness before toggling irradiation on.

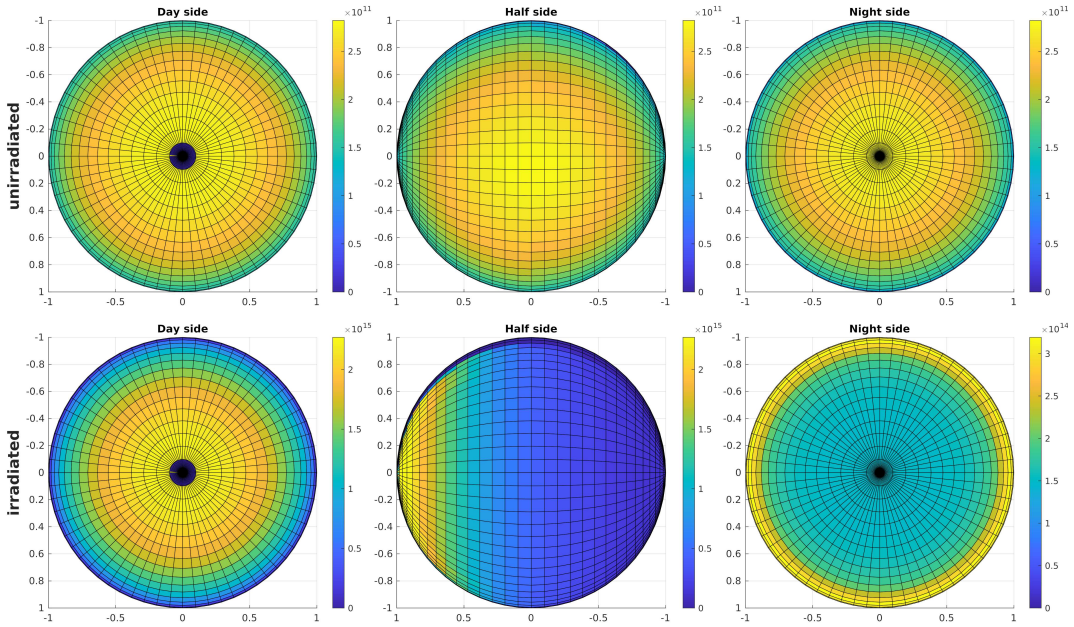

Figure 4.15: 3D intensities for H_α without (upper row) and with (lower row) irradiation from three different observer perspectives (full dayside in the first column, half day half night in the second column and full nightside in the third column). Note that the colorbar scale changes.

Figure 4.15 depicts the difference in intensity at H_α central line (λ = 6562 Å) between an isolated secondary and one irradiated by a blackbody of 42,000 K for three different observer perspectives (full dayside, sideways where half of the visible hemisphere is at night and half at day, later referred to as half side, and full nightside). The isolated star case (upper row) is radialsymmetric and except for resolution effects as seen at half side the intensity structure looks exactly the same from all perspectives. Limb darkening effects are clearly visible. On the contrary, the irradiated case (lower row) is, as expected, not overall radially symmetric. The substellar point with the

hotspot is well visible on the dayside of the irradiated secondary. The black center is a mapping error. Please also note, that the colorbar scale changes for the nightside of the irradiated secondary in order to see more features on this overall darker side. However, the nightside for the irradiated case still displays much higher intensities than the unirradiated case. A remarkable feature at this nightside for the irradiated secondary is the bright ring. This is due to the radiation from the primary that shines through the outer atmosphere layers (transmission spectrum).

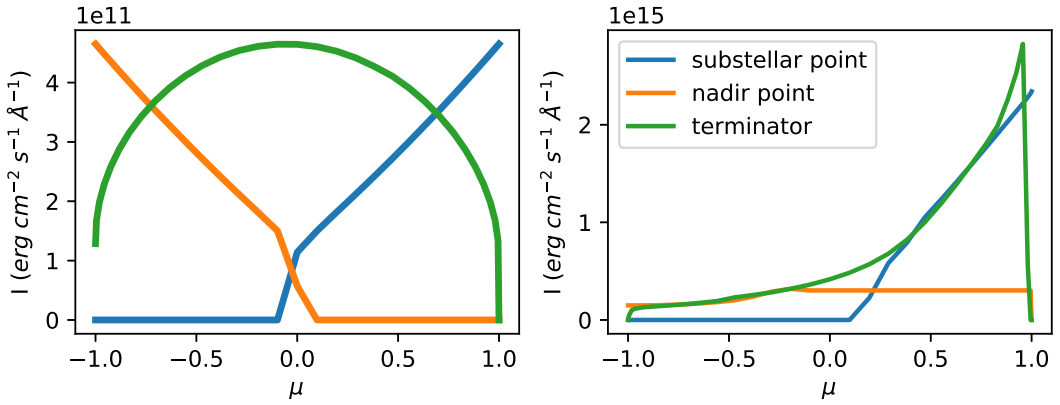

Figure 4.16: Intensities at H_α for unirradiated and irradiated secondary with PHOENIX/3D for the substellar point (blue), the terminator point at $\phi = 0°$ (green) and the nadir point (orange) with respect to the observer angle μ_{obs} ($\mu_{obs} = 1$ points in the direction of the primary, $\mu_{obs} = -1$ points in the oposite direction and $\mu_{obs} = 0$ points laterally away of the secondary in $\theta = 90°; \phi = 0°$ direction).

In Figure 4.16 the intensities for H_α are shown for three different points on the sphere: the substellar point (blue), the terminator at $\phi = 0$ (green) and directly on the opposite of the substellar point, here referred to as nadir point (orange), for different observer perspectives $\mu_{obs} = \cos\omega$ ($\mu_{obs} = 1$ points towards the primary, $\mu_{obs} = -1$ is coming from the primary, and $\mu_{obs} = 0$ is in the direction of the surface normal at the terminator at $\phi = 0$). The isolated model is shown in the left panel of this figure. Only intensities for μ_{obs} angles that are visible to the observer have values different to zero, because PHOENIX/3D calculates the intensities as seen from an observer and hence, only radiation facing the observer is different from zero. With the green terminator profile

the arc shows the limb darkening effects with maximal contribution in the direction of the surface normal. Also for the other two lines the maximal intensity is in the direction of the surface normal ($\mu_{\text{obs}} = 1$ for the substellar point and $\mu_{\text{obs}} = -1$ for the nadir point). This is completely different when toggling irradiation mode. The dominant primary contribution is added to the intrinsic intensities resulting in an increase up to four orders of magnitude. While the trend for the substellar point still resembles the unirradiated one, huge variations are revealed for the terminator and nadir point. There is a rise for the terminator point even before $\mu_{\text{obs}} = 0$ and a steep rise when approaching the direction towards the primary star ($\mu_{\text{obs}} = 1$). The intensities for the nadir point are almost isotropic to all μ_{obs} angles. These are effects of transmission in the atmosphere near the terminator and scattering.

Figure 4.17 depicts the intensities for irradiated secondaries for selected wavelengths between 2,000 and 8,000 Å. The size of the hotspot at the substellar point increases while the ring of transmission on the nightside decreases with larger wavelengths (note that also here the scale of the colorbar changes and the mapping error at the substellar point persists).

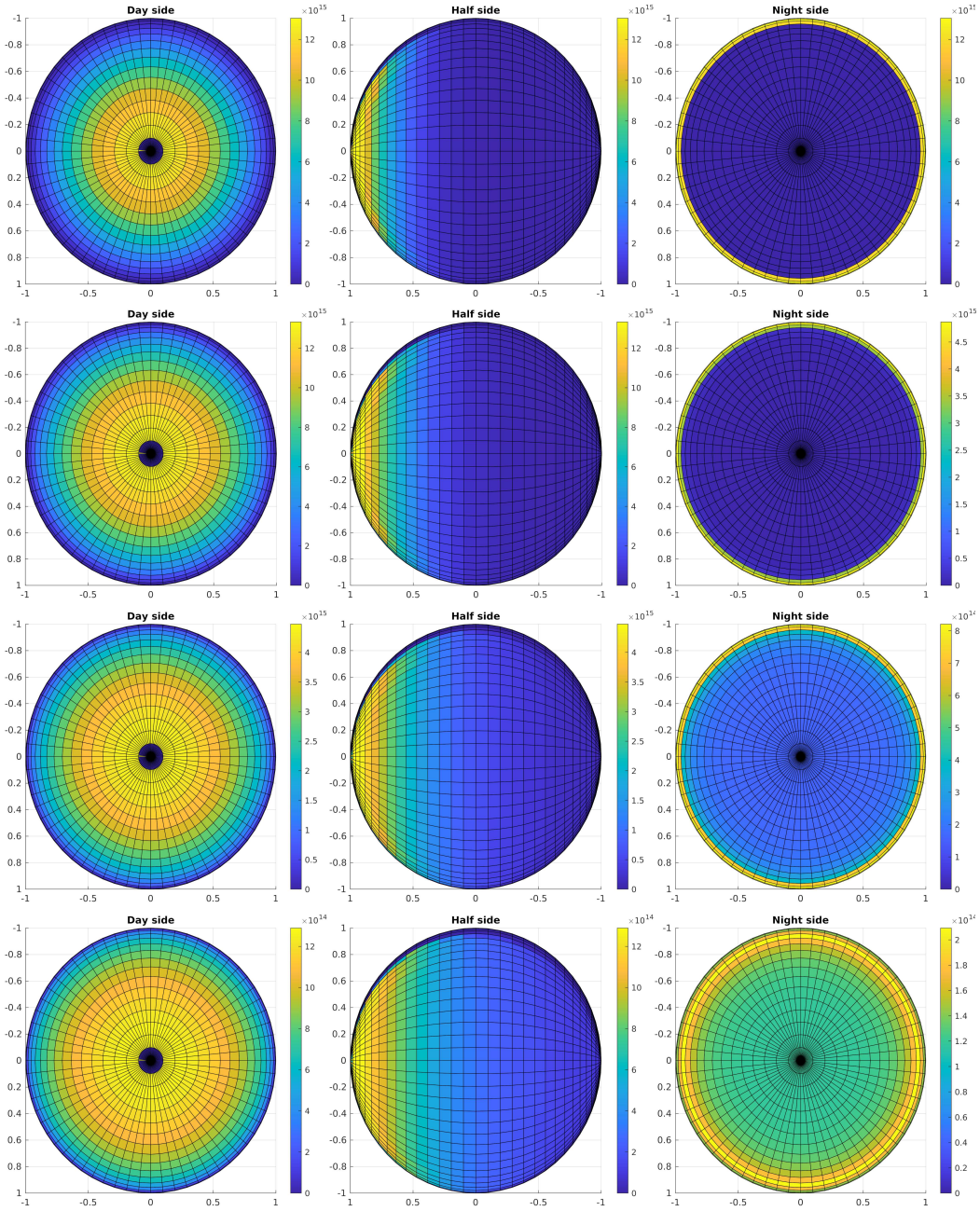

Figure 4.17: Intensities for an irradiated secondary in 3D at wavelengths 2000, 3000, 5000 and 8000 Å (from top to bottom row) for three different observer perspectives. Note that the scale of the colorbar changes.

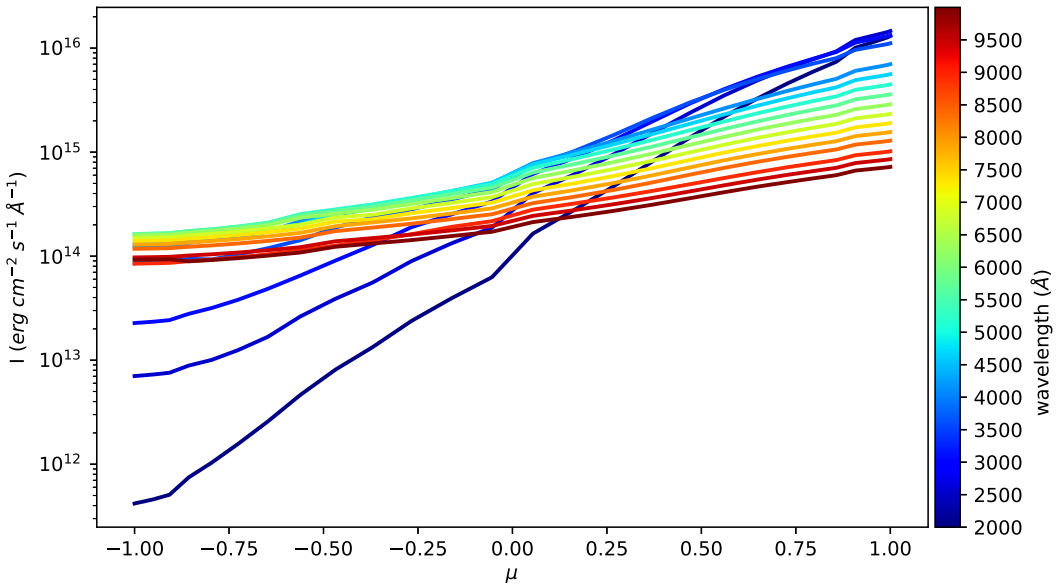

Figure 4.18: Intensities for a 3D irradiated secondary at selected wavelengths between 2,000 Å (dark blue) and 10,000 Å (dark red) for different observer angles μ_{obs} for ($\theta = \arccos(\mu_{\text{obs}})$, $\phi = 0$) in the direction of the surface normal. An observer with $\mu_{\text{obs}} = -1$ looks straight at the nadir point, with $\mu_{\text{obs}} = 0$ onto the terminator, and with $\mu_{\text{obs}} = +1$ straight onto the substellar point.

Figure 4.18 shows the intensities for a 3D irradiated secondary for wavelengths between 2,000 and 10,000 Å for intensities at different observer perspectives μ_{obs} but this time the radially outward pointing intensity is shown from the nadir point towards the substellar point for $\phi = 0$. While the intensities of higher wavelengths do not change much with observer perspective, the gradient between day- and nightside increases with a decrease of wavelength. This is most extreme for 2,000 Å where the difference is bigger than five orders of magnitudes. This arises because of backscattering effects and the increase of temperatures on the dayside of the secondary, resulting in a shift towards lower wavelengths.

4.3 1.5D to 3D Comparison

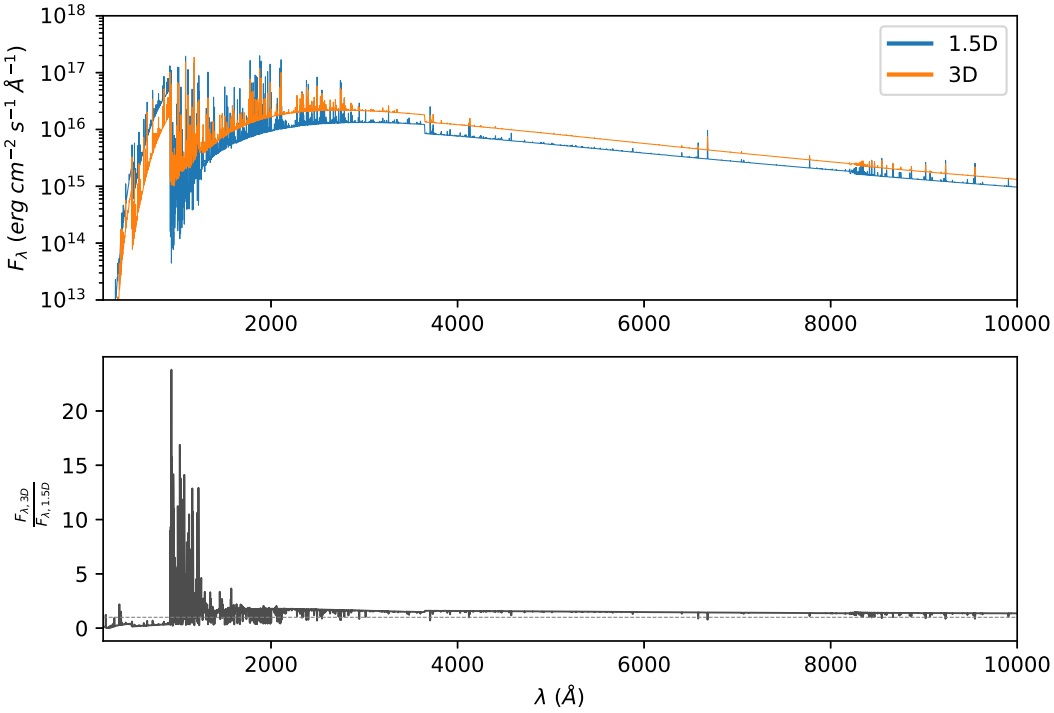

Figure 4.19: Comparison of 1.5D and 3D spectra of an irradiated secondary. Absolute flux values are plotted in the upper figure, while the ratio of 3D to 1.5D is shown in the lower figure.

In Figure 4.19 the difference in absolute flux between our 1.5D and 3D dayside results is shown. The upper panel represents absolute flux values. There is a slight offset between 1.5D and 3D but they are still very close as can be seen in the lower panel of this figure where the ratio of the two results is plotted. Characteristic peaks are slightly deeper in the 1.5D results.

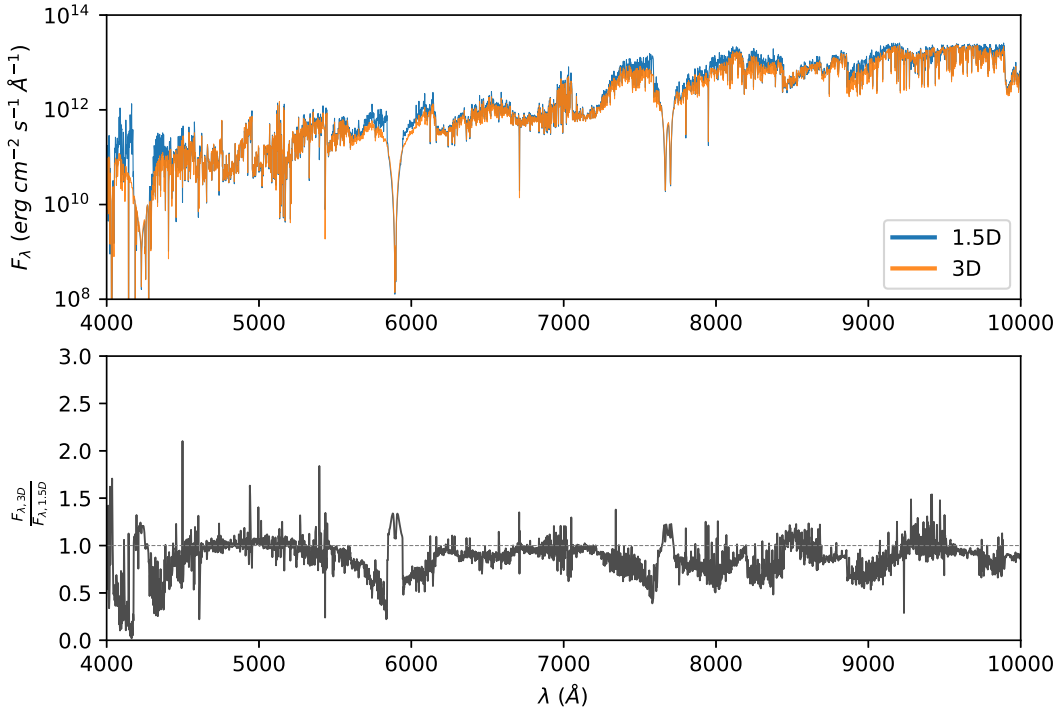

Figure 4.20: Comparison of 1.5D and 3D spectra of an unirradiated secondary. Absolute flux values are plotted in the upper figure, while the ratio of 3D to 1.5D is shown in the lower figure.

The same is shown in Figure 4.20 for an unirradiated secondary. These two curves match quite good as well, but the small offset between the two curves is smaller in 3D than the 1.5D at shorter wavelengths and vice versa for wavelengths above 1,300 Å. The ratio of 3D to 1.5D is shown in the lower figure of this plot. Interestingly, also here are more emission lines clearer visible in 1.5D.

Exemplarily, the 1.5D intensities are compared to 3D intensities for a wavelength of 5,000 Å in Figure 4.21. The day- and halfside of the secondary show a bright ring near the terminator caused by the artificial 1D results as analyzed in Section 4.1.1. However, the nightside has a very dark limb in contrast to the 3D model, because 1.5D is not able to account for the transmission of light in these regions.
This is a remarkable advantage of the 3D results.

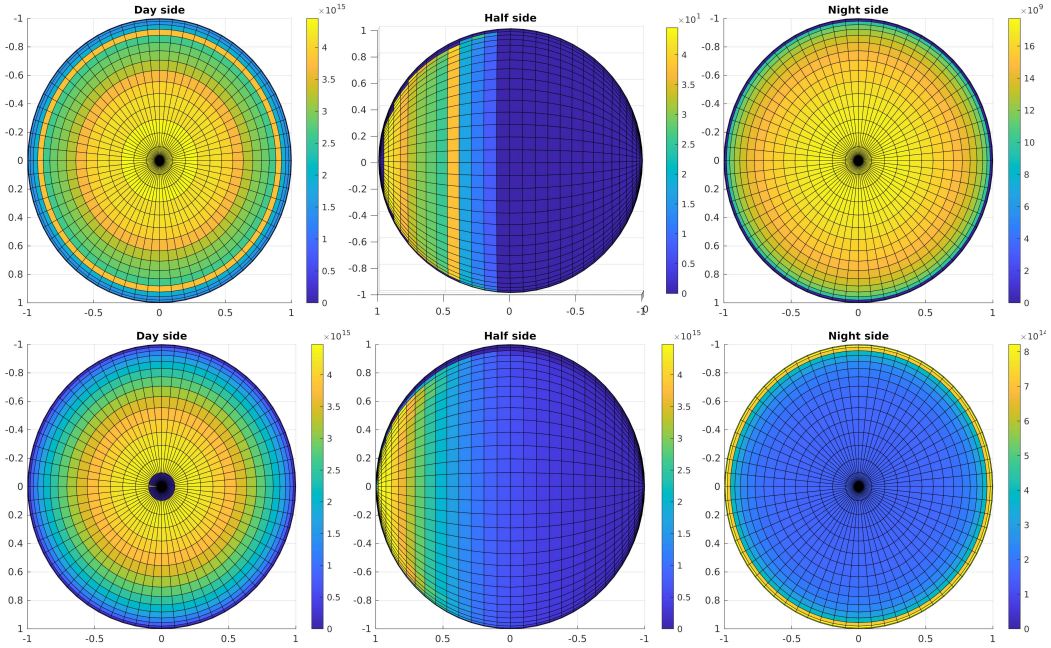

Figure 4.21: Comparision of 1.5D (upper row) and 3D (lower row) intensities at 5000 Å for three observer perspectives.

5 Summary & Future Prospects

As a step towards modelling the atmosphere of close binary stars and irradiated planets we have presented 1.5D and 3D PHOENIX LTE models for the close binary star system AA Dor as a prove of concept. Out of several PHOENIX/1D models with and without external irradiation we have calculated so-called 1.5D spectra and have produced a 1.5D hydrostatic structure that has been used as an input for the PHOENIX/3D models. We have generated 3D models and have calculated 3D spectra.

With the 1D models a slight atmosphere expansion due to local heating was found. Both 1.5D and 3D models were able to reproduce different observer perspectives. Limits for the 1.5D models were found near the terminator regions where 1D models fail to process the radiation under low incident angles due to a lack of horizontal interactions. However, the 3D models are able to account for this and so transmission features at the limb of the nightside were found. Seven of the eleven identified secondary lines in the visual range listed in Hoyer et al. (2015) were found in these spectra and a dozen more lines were suggested.

A very important next step are further comparisons to observations. A lot of observational data for AA Dor can be found in various archives. Most recently, Hoyer et al. (2015) presented secondary signatures in UVES and XSHOOTER observations. These spectra have much better resolutions than our model so far, so the resolution in wavelength of our model needs be increased accordingly. And as the secondary is highly inhomogeneous (e.g., in temperature structure as elaborated in Section 4.1.1) convenient assumptions underlying the simple LTE description may break and it will be highly desirable to run the models in NLTE.

It would be also very interesting to compare these results to the theoretical model

of Vučković et al. (2016). Also, a primary model with the same spectral resolution should be calculated in order to be able to compare the results of this model to the hardly separable binary star spectrum observations. Additionally, this primary spectrum can be used instead of the blackbody as the irradiation input for the secondary. When modeling the primary it might also be interesting to study the effects of two-way irradiation. The primary also receives irradiation by the secondary, which by itself is influenced by the primary irradiation. So ultimately, the irradiation effect on one another needs to be iterated self-consistently. While this is merely interesting for a binary star like AA Dor that has a very dominant component, this strictly becomes necessary if both components are more similar to each other.

Furthermore, the number of irradiation angles in the 1.5D approach could be increased, resulting in a hydrostatic structure with a higher resolution. As mentioned in the analysis of Figure 4.1 the entropy in depth of the 1.5D secondary star should be matched as described in Brett and Smith (1993). To distinguish the irradiation effects resulting from the heating up of the atmosphere and those of back scattering, the results of an irradiated 1.5D hydro structure run in unirradiated 3D mode and one run in irradiated mode can be compared.

Due to the limitations of the PHOENIX/1D models to include horizontal voxel coupling, it should be considered to calculate the hydrodynamic input structure for PHOENIX/3D in full 3D, for instance with CO^{5}BOLD (Freytag et al., 2012), a 3D radiation chemo-magneto-hydrodynamics code, MURaM (Vögler et al., 2005), the Stagger-Grid (Magic et al., 2013), or FLASH (Fryxell et al., 2000).

With the steep temperature gradients occurring on the secondary it is very plausible that lateral winds are present. Thus, it would be very fascinating to include global circulation models. The occurrence of radiation-driven horizontal motions for instance for irradiated substellar objects like brown dwarfs and hot Jupiters is already a topic of research (e.g. Lee et al. (2020), Tan and Showman (2020), Showman et al. (2019)). They found numerous zonal eastward and westward jets transporting the

heat of the dayside all across the secondary. Also, often due to these jets the hotspot is slightly shifted from the substellar point in the direction of the jet.
Especially the nightside of the secondary can be so cold that clouds could form. PHOENIX is able to include this with its DRIFT mode (Dehn, 2007).

The transition from stellar companions towards planets brings about further complications. In fact, already for brown dwarfs the assumption of a simple chemical equilibrium and homogeneous distribution of elements across the entire atmosphere steadily breaks down (as a combined result of condensation, precipitation and turbulent mixing) and thus, chemical rate equations would need to be solved (Hubeny and Burrows, 2007; Barman et al., 2011).
Aspects like planet evolution, i.e., formation and cooling history and migration, as well as rain-out and mixing of heavy elements, also have an influence on atmospheric compositions and thus, can have a huge impact on the understanding of observations. And when modelling rocky planets the interaction of the solid surface and the atmosphere needs to be included. Rocky planets can have volcanism, which would need to involve hydro-simulations of the planetary core and mantle in order to compute consistent atmospheres (Robock and Oppenheimer, 2003; Valentine and Bossert, 1998). And when a biosphere is present this will change the atmosphere extremely, as found in Earth's atmosphere history (Kasting and Siefert, 2002).

This is of course by far not an exhaustive list of possible extensions to our atmosphere models. But it gives a good impression that the research on atmosphere models is far from being done. As the computing power has increased rapidly within the last decade, the journey seems to have just started towards even more elaborated atmosphere models in future when even more computational resources will become available.

Bibliography

Baran, A. S., Østensen, R. H., Heber, U., Irrgang, A., Sanjayan, S., Telting, J. H., Reed, M. D., and Ostrowski, J. (2021). Space observations of AA Doradus provide consistent mass determinations. New HW-Vir systems observed with TESS. *MNRAS*, 503(2):2157–2167.

Barman, T. S. (2002). *Irradiated Model Atmospheres for Extrasolar Giant Planets and Secondary Stars of Pre-Cataclysmic Variables*. PhD thesis, The University of Georgia.

Barman, T. S., Macintosh, B., Konopacky, Q. M., and Marois, C. (2011). Clouds and Chemistry in the Atmosphere of Extrasolar Planet HR8799b. *ApJ*, 733(1):65.

Böhm-Vitense, E. (1989). *Introduction to Stellar Astrophysics. Vol.2. Stellar atmospheres*. ISBN: 978-051162301-1.

Brett, J. M. and Smith, R. C. (1993). A model atmosphere investigation of the effects of irradiation on the secondary star in a dwarf nova. *MNRAS*, 264:641.

Cannon, C. J. (1973). Angular quadrature perturbations in radiative transfer theory. *J. Quant. Spec. Radiat. Transf.*, 13(7):627–633.

Chabrier, G. and Baraffe, I. (2000). Theory of Low-Mass Stars and Substellar Objects. *ARA&A*, 38:337–377.

Conti, P. S., Dearborn, D., and Massey, P. (1981). Analysis of HDE 269696 0 LB 3459, an O-type subdwarf eclipsing binary system. *MNRAS*, 195:165–172.

Corcoran, K. A., Barlow, B., Walser, S., Mycroft, S., Aube, J., Ratzloff, J., Law, N., Corbett, H. T., Howard, W. S., and Fors, O. (2019). Evryscope Observations of Post-Common-Envelope Hot Subdwarf Systems. In *American Astronomical*

Society Meeting Abstracts #233, volume 233 of *American Astronomical Society Meeting Abstracts*, page 360.16.

Dehn, M. (2007). *Self-consistent Dust Modelling in Brown Dwarfs*. PhD thesis, Universität Hamburg.

Fleig, J., Rauch, T., Werner, K., and Kruk, J. W. (2008). FUSE spectroscopy of the sdOB primary of the post common-envelope binary LB 3459 (AA Doradus). *A&A*, 492(2):565–573.

Freytag, B., Steffen, M., Ludwig, H. G., Wedemeyer-Böhm, S., Schaffenberger, W., and Steiner, O. (2012). Simulations of stellar convection with CO5BOLD. *Journal of Computational Physics*, 231(3):919–959.

Fryxell, B., Olson, K., Ricker, P., Timmes, F. X., Zingale, M., Lamb, D. Q., MacNeice, P., Rosner, R., Truran, J. W., and Tufo, H. (2000). FLASH: An Adaptive Mesh Hydrodynamics Code for Modeling Astrophysical Thermonuclear Flashes. *ApJS*, 131(1):273–334.

Hauschildt, P. H., Barman, T. S., Baron, E., and Allard, F. (2003). Temperature Correction Methods. In Hubeny, I., Mihalas, D., and Werner, K., editors, *Stellar Atmosphere Modeling*, volume 288 of *Astronomical Society of the Pacific Conference Series*, page 227.

Hauschildt, P. H. and Baron, E. (2006). A 3D radiative transfer framework. I. Non-local operator splitting and continuum scattering problems. *A&A*, 451(1):273–284.

Hauschildt, P. H. and Baron, E. (2009). A 3D radiative transfer framework. IV. Spherical and cylindrical coordinate systems. *A&A*, 498(3):981–985.

Hauschildt, P. H. and Baron, E. (2010). A 3D radiative transfer framework. VI. PHOENIX/3D example applications. *A&A*, 509:A36.

Heber, U. (2016). Hot Subluminous Stars. *PASP*, 128(966):082001.

Heber, U., Hunger, K., Rauch, T., and Werner, K. (1988). Improved non-lte model atmospheres for subluminous o-stars. *Symposium - International Astronomical Union*, 132:117–122.

Hilditch, R. W. (2001). *An Introduction to Close Binary Stars*.

Hilditch, R. W., Kilkenny, D., Lynas-Gray, A. E., and Hill, G. (2003). New VI_C photometry of the sdOB binary AA Dor and an improved photometric model. *MNRAS*, 344(2):644–650.

HLRN (2001). Supercomputer system of the north german supercomputing alliance. www.hlrn.de/. Accessed: 2020-03-20.

Hoyer, D., Rauch, T., Werner, K., Hauschildt, P. H., and Kruk, J. W. (2015). Search with UVES and X-Shooter for signatures of the low-mass secondary in the post common-envelope binary AA Doradus. *A&A*, 578:A125.

Hubeny, I. and Burrows, A. (2007). A systematic study of departures from chemical equilibrium in the atmospheres of substellar mass objects. *ApJ*, 669(2):1248–1261.

Hubeny̋, I. and Mihalas, D. (2015). *Theory of Stellar Atmospheres: An Introduction to Astrophysical Non-equilibrium Quantitative Spectroscopic Analysis*. Princeton series in astrophysics. Princeton University Press. ISBN: 978-069116329-1.

Hummel (2015). Supercomputer System of the Regional Computing Center at the University of Hamburg. www.rrz.uni-hamburg.de/services/hpc/hummel-2015.html. Accessed: 2021-03-20.

Johnas, C. M. S. (2007). *Non-Analytical Line Profiles in Stellar Atmospheres For Planetary Host Star Systems*. PhD thesis, Universität Hamburg.

JPL (2005). Nasa's spitzer marks beginning of new age of planetary science. http://www.spitzer.caltech.edu/news/189-ssc2005-09-NASA-s-Spitzer-Marks-Beginning-of-New-Age-of-Planetary-Science. Accessed: 2020-11-10.

Kallrath, J. and Milone, E. F. (2009). *Eclipsing Binary Stars: Modeling and Analysis*.

Kasting, J. F. and Siefert, J. L. (2002). Life and the evolution of earth's atmosphere. *Science*, 296(5570):1066–1068.

Kilkenny, D. (2011). The orbital periods of AA Dor and NY Vir. *MNRAS*, 412(1):487–491.

Kilkenny, D. (2014). The orbital periods of three sdB eclipsing binary systems. *MNRAS*, 445(4):4247–4251.

Kilkenny, D., Hilditch, R. W., and Penfold, J. E. (1978). LB 3459, a short-period eclipsing binary system containing two O-type subdwarfs. *MNRAS*, 183:523–531.

Kilkenny, D. and Hill, P. W. (1975). Photometry of faint blue stars. *MNRAS*, 173:625–636.

Kilkenny, D., Hill, P. W., and Penfold, J. E. (1981). LB 3459, an O-type subdwarf eclipsing binary system. III. Radial velocity curve and orbital solutions. *MNRAS*, 194:429–437.

Kilkenny, D., Penfold, J. E., and Hilditch, R. W. (1979). LB 3459, an O-type subdwarf eclipsing binary system - II. New photometry and an improved analysis. *MNRAS*, 187:1.

Kirkpatrick, J. D., Reid, I. N., Liebert, J., Cutri, R. M., Nelson, B., Beichman, C. A., Dahn, C. C., Monet, D. G., Gizis, J. E., and Skrutskie, M. F. (1999). Dwarfs

Cooler than “M“: The Definition of Spectral Type “L” Using Discoveries from the 2 Micron All-Sky Survey (2MASS). *ApJ*, 519(2):802–833.

Klepp, S. and Rauch, T. (2011). On the sdOB primary of the post common-envelope binary AA Doradus (LB 3459). *A&A*, 531:L7.

Kudritzki, R. P., Simon, K. P., Lynas-Gray, A. E., Kilkenny, D., and Hill, P. W. (1982). LB 3459 - an O-type subdwarf eclipsing binary system. Non-LTE analysis of the primary. *A&A*, 106:254–260.

Lee, G. K. H., Casewell, S. L., Chubb, K. L., Hammond, M., Tan, X., Tsai, S.-M., and Pierrehumbert, R. T. (2020). Simplified 3D GCM modelling of the irradiated brown dwarf WD 0137-349B. *MNRAS*, 496(4):4674–4687.

Lucy, L. B. (1964). A Temperature-Correction Procedure. *SAO Special Report*, 167:93.

Lynas-Gray, A. E., Heber, U., Kudritzki, R. P., and Simon, K. P. (1984). Limb-darkening and metal abundances in the sdOB primary of the eclipsing binary LB 3459 (AA Dor). In Rolfe, E., editor, *Fourth European IUE Conference*, volume 218 of *ESA Special Publication*, pages 285–189.

Magic, Z., Collet, R., Asplund, M., Trampedach, R., Hayek, W., Chiavassa, A., Stein, R. F., and Nordlund, Å. (2013). The Stagger-grid: A grid of 3D stellar atmosphere models. I. Methods and general properties. *A&A*, 557:A26.

Mihalas, D. (1970). *Stellar atmospheres*. ISBN: 978-071670333-4.

NASA (2011). Astronomers find elusive planets in decade-old hubble data. https://www.nasa.gov/mission_pages/hubble/science/elusive-planets.html. Accessed: 2020-11-10.

NASA (2014). Astronomical forensics uncover planetary disks in nasa's hubble archive. https://www.nasa.gov/press/2014/april/astronomical-forensics-uncover-planetary-disks-in-nasas-hubble-archive/. Accessed: 2020-11-10.

NASA (2021). Exoplanet exploration. https://exoplanets.nasa.gov/discovery/exoplanet-catalog/. Accessed: 2021-04-14.

Paczynski, B. and Dearborn, D. S. (1980). Evolutionary model of the subdwarf binary system LB 3459. *MNRAS*, 190:395–402.

Rauch, T. (2000). NLTE spectral analysis of the sdOB primary of the eclipsing binary system LB 3459 (AA Dor). *A&A*, 356:665–675.

Rauch, T. and Werner, K. (2003). The rotational velocity of the sdOB primary of the eclipsing binary system LB 3459 (AA Dor). *A&A*, 400:271–277.

Rauch, T. and Werner, K. (2011). AA Dor Animations. http://astro.uni-tuebingen.de/~rauch/lb3459.html. Accessed: 2021-03-09.

Robock, A. and Oppenheimer, C. (2003). *Volcanism and the Earth's Atmosphere*. ISBN: 978-087590998-1.

Rutten, R. J. (2003). *Radiative Transfer in Stellar Atmospheres*.

Schaffenroth, V., Barlow, B., Geier, S., Vučković, M., Kilkenny, D., and Schaffenroth, J. (2017). News From The Erebos Project. *Open Astronomy*, 26(1):208–213.

Showman, A. P., Tan, X., and Zhang, X. (2019). Atmospheric Circulation of Brown Dwarfs and Jupiter- and Saturn-like Planets: Zonal Jets, Long-term Variability, and QBO-type Oscillations. *ApJ*, 883(1):4.

Silvotti, R., Schaffenroth, V., Heber, U., Østensen, R. H., Telting, J. H., Vos, J., Kilkenny, D., Mancini, L., Ciceri, S., Irrgang, A., and Drechsel, H. (2021). EPIC 216747137: a new HW Vir eclipsing binary with a massive sdOB primary and a low-mass M-dwarf companion. *MNRAS*, 500(2):2461–2474.

Sozzetti, A. (2010). Astrometry and Exoplanets: The Gaia Era and Beyond. In *EAS Publications Series*, volume 45 of *EAS Publications Series*, pages 273–278.

Tan, X. and Showman, A. P. (2020). Atmospheric Circulation of Tidally Locked Gas Giants with Increasing Rotation and Implications for White Dwarf-Brown Dwarf Systems. *ApJ*, 902(1):27.

Unsöld, A. and Baschek, B. (2001). *The new cosmos : an introduction to astronomy and astrophysics*. ISBN: 978-354067877-9.

Valentine, G. A. and Bossert, J. E. (1998). Numerical simulation of explosive volcanism and its effects on the atmosphere.

Vögler, A., Shelyag, S., Schüssler, M., Cattaneo, F., Emonet, T., and Linde, T. (2005). Simulations of magneto-convection in the solar photosphere. Equations, methods, and results of the MURaM code. *A&A*, 429:335–351.

Vučković, M., Østensen, R. H., Németh, P., Bloemen, S., and Pápics, P. I. (2016). Looking on the bright side: The story of AA Doradus as revealed by its cool companion. *A&A*, 586:1–12.

Vučković, M., Østensen, R., Bloemen, S., Decoster, I., and Aerts, C. (2008). Orbital Effects in VLT–UVES Spectra of AA Dor and NY Vir. In Heber, U., Jeffery, C. S., and Napiwotzki, R., editors, *Hot Subdwarf Stars and Related Objects*, volume 392 of *Astronomical Society of the Pacific Conference Series*, page 199.

Wichert, V. (2018). *Numerical Radiation Transport Algorithms for Emergent Computer Architectures*. PhD thesis, Universität Hamburg.

Włodarczyk, K. (1984). The secondary component of AA Doradus. *Acta Astron.*, 34:381–385.

Wolszczan, A. and Frail, D. A. (1992). A planetary system around the millisecond pulsar PSR1257 + 12. *Nature*, 355(6356):145–147.

Wolz, M., Kupfer, T., Drechsel, H., Heber, U., Irrgang, A., Hermes, J. J., Bloemen, S., Levitan, D., Dhillon, V., and Marsh, T. (2018). Spectroscopic and Photometric Analysis of the HW Vir Star PTF1 J011339.09+225739.1. *Open Astronomy*, 27(1):80–90.

Yang, J., Boué, G., Fabrycky, D. C., and Abbot, D. S. (2014). Strong Dependence of the Inner Edge of the Habitable Zone on Planetary Rotation Rate. *ApJL*, 787(1):L2.

Acknowledgement

I would like to express my deepest thanks to Peter for giving me the opportunity to work on this project. With all the ups and downs these years have been a wonderful experience for me. Many thanks to the DFG for funding this project with the title *Spektralanalyse des Sekundärsternes des AA Dor Systems mit PHOENIX/3D* (HA 34573-1).

I would also like to extend my deepest gratitude to Peter, Travis and Eddie for making my visit to the University of Arizona and the University of Oklahoma possible. It was an amazing time and I returned filled with new experiences and with a new motivation for science.

Many thanks to Andreas for his company and his help with proofreading. I gratefully acknowledge the company of Simon. I enjoyed our strolls in the nature around the observatory and our thriving conversations.

I cannot begin to express my thanks to Sören. He provided me with encouragement and always had an open ear for me throughout my time at the observatory. He endured countless questions and was very persevering when it came to proofread my thesis.

I am also indebted to Jannis. His support and understanding during this time as well as his English grammar expertise is heartily appreciated.

Finally, I would like to thank all my friends and family for believing in me and for always being there for me.

Eidesstattliche Versicherung/ Declaration on Oath

Hiermit versichere ich an Eides statt, die vorliegende Dissertationsschrift selbst verfasst und keine anderen als die angegebenen Hilfsmittel und Quellen benutzt zu haben.

Die eingereichte schriftliche Fassung entspricht der auf dem elektronischen Speichermedium.

Die Dissertation wurde in der vorgelegten oder einer ähnlichen Form nicht schon einmal in einem früheren Promotionsverfahren angenommen oder als ungenügend beurteilt.

Hamburg, den 22. 06. 2021

Fiona Dorothea Elisabeth Prodöhl